Chiral-perovskite optoelectronics

Guankui Long [ID][1,8], *Randy Sabatini* [ID][2,8], *Makhsud I. Saidaminov* [ID][3,4,8], *Girish Lakhwani* [ID][2], *Abdullah Rasmita* [ID][1], *Xiaogang Liu*[5], *Edward H. Sargent* [ID][3 ✉] *and Weibo Gao* [ID][1,6,7 ✉]

Abstract | Hybrid organic–inorganic perovskites (HOIPs) offer long carrier-diffusion lengths, high absorption coefficients, tunable band gaps and long spin lifetimes. The flexible crystal structure and ionic nature of HOIPs make it possible to allow tuning of their material properties through rational design, including the incorporation of chiral organic ligands. Recently, chiral HOIPs have emerged as promising materials for chiroptoelectronics, spintronics and ferroelectrics. They exhibit high photoluminescence polarization (17% without an external magnetic field), good device performance (a circularly polarized photodetector had 100 times higher responsivity than one based on a chiral metasurface) and high saturated polarization (~2 times higher than that of barium titanate). Here, we review the latest advances in chiral HOIPs and investigate the specific benefits of combining chiral organic and inorganic components in perovskites. We discuss demonstrations of chiroptical and ferroelectric applications, and conclude with our perspective on the future opportunities for chiral HOIPs.

In the past decade, hybrid organic–inorganic perovskites (HOIPs) have become an important materials family for optoelectronics. Low trap densities[1] and long carrier-diffusions lengths[2–5] have led to solar cells with efficiency above 20%[6–9]; near-unity photoluminescence quantum yields and tunable emission have enabled high-performing light-emitting diodes (LEDs) spanning the visible and portions of the near-infrared spectra[10–12]; and large optical gain has allowed low thresholds in both pulsed and continuous-wave optically pumped lasing[13–17]. With high mobilities[18–21] and dielectric constants[22], these materials have also been explored as photodetectors[23,24]. In addition, their large Rashba splitting[25,26] and long spin lifetimes[27–29] have motivated research into spintronic applications[30–32].

HOIPs possess a flexible crystal structure and a tunable hybrid organic–inorganic composition. This enables the incorporation of chiral ligands[33–37], which allow perovskites to be used in chiroptoelectronic[38,39], ferroelectric[40–42] and chiro-spintronic[43,44] applications.

Chirality and its extension to perovskites

A material is chiral if its mirror image cannot be brought to coincide with it[45]. Chirality is found in the ʟ-configuration of the natural α-amino acids except glycine and in the ᴅ-configuration of the saccharides and saccharide units in cellulose, starch and DNA. In addition, chiral templates and sites play an important role in biological recognition and assembly. The community has harnessed this property, for example, in chiral catalysts that are widely employed in asymmetric synthesis of pharmaceuticals.

Based on non-centrosymmetric structures, chiral materials can exhibit optical rotation[46], circular dichroism[47], second-harmonic generation (SHG)[48], piezoelectricity[40], pyroelectricity[49], ferroelectricity[50] and topological quantum properties[51]. Thus, chiral materials have potential for application in chiroptoelectronics, including in circularly polarized light (CPL) photodetectors[52–55], circularly polarized LEDs[56–60], bioresponsive imaging[61–63], 3D displays[64,65], as well as applications in quantum computing[66,67], quantum communication[68–70], non-volatile-memory devices[71] and spintronics[30,43,44,72] (FIG. 1).

Chiroptical effects can be reproduced by incorporating metasurfaces and optical elements (such as quarter-wave plates); however, some applications require chiral materials. Optical elements decrease efficiency, and metasurfaces increase the complexity, and often cost, of a system. Chiral materials offer an advantage in applications requiring small footprints and ease of fabrication. In many of the applications listed above (such as on-chip circularly polarized photodetectors[52–55], LEDs[73,74] and polarization-based memory storage[75,76]), additional elements hinder fabrication and performance; thus, true chiral materials are required.

The first demonstration of chirality in HOIPs was a 1D chiral-perovskite single crystal in 2003 (REF.[33]), with 2D chiral-perovskite single crystals following in 2006 (REF.[34]) (FIG. 2). However, their chiroptical properties were not explored initially. Only after breakthroughs in the power-conversion efficiency of perovskite solar cells[77,78] did investigation begin into many aspects of their optical properties[14–16]. Chiral perovskites re-emerged in

2017, when the first chiroptical study was performed[47]. Since then, additional chiral HOIPs have been reported, including chiral-perovskite nanocrystals[79,80], cogels[81], nanoplatelets[82] and low-dimensional chiral perovskites[83]. Whereas metal-free 3D chiral perovskites have been synthesized[84], metal-containing 3D chiral HOIPs have yet to be demonstrated, although they have been theoretically predicted to be both thermodynamically and kinetically stable[85].

Chiral perovskites are classified into 65 different space groups, known as the Sohncke space groups[86], and exhibit chiroptical and ferroelectric properties according to the Neumann–Curie principle[87,88] (FIG. 3). In BOX 1, we define key terms that are used throughout this Review to discuss chiroptical and ferroelectric properties of chiral perovskites (see also Section 1 of the Supplementary Information for a more detailed description).

The optical and electronic properties of chiral perovskites have been recently reviewed[89]; in the present Review, we focus on their structure–property relationships. We also discuss the motivation for incorporating chiral HOIPs and cover chiroptical effects[46,90] and ferroelectricity[50,91], as well as the concepts underlying chiral induction (that is, chirality transfer)[92,93]. We then review applications such as circularly polarized photodetection[38], spin manipulation[39,83], high-order nonlinear chiroptical effects[48,80] and ferroelectricity[40,41]. We close with a forward-looking perspective on chiral HOIPs.

Design of chiral perovskites

When a perovskite material incorporates chiral organic molecules, they can impart their chiral properties to it[92]. This chirality transfer can be mediated through the formation of chemical bonds or even through spatial interactions between a chiral and an achiral system[92,93]. TABLE 1 summarizes the different chirality-transfer mechanisms in chiral HOIPs[47,82,94]. They include: ligand-induced chiral inorganic structure (I, such as in chiral-perovskite single crystals)[33,34]; chiral distortion of the inorganic surface (II, such as in chiral-perovskite nanocrystals)[79,80]; chiral patterning of the surface ligands[95,96] (III); and electronic coupling between the chiral organic molecules and the inorganic structure (IV, chiral field effect)[97,98].

Author addresses

[1]Division of Physics and Applied Physics, School of Physical and Mathematical Sciences, Nanyang Technological University, Singapore, Singapore.
[2]ARC Centre of Excellence in Exciton Science, School of Chemistry, University of Sydney, Sydney, New South Wales, Australia.
[3]Department of Electrical and Computer Engineering, University of Toronto, Toronto, Ontario, Canada.
[4]Department of Chemistry and Electrical & Computer Engineering, Centre for Advanced Materials and Related Technologies (CAMTEC), University of Victoria, Victoria, British Columbia, Canada.
[5]Department of Chemistry, National University of Singapore, Singapore, Singapore.
[6]MajuLab, CNRS-Université de Nice-NUS-NTU International Joint Research Unit UMI, Singapore, Singapore.
[7]The Photonics Institute and Centre for Disruptive Photonic Technologies, Nanyang Technological University, Singapore, Singapore.
[8]These authors contributed equally: Guankui Long, Randy Sabatini, Makhsud I. Saidaminov

Chirality through chiral ligands

Direct synthesis. Chiral perovskites can be synthesized directly using chiral ligands to introduce chirality (FIG. 4a), enabling 0D, 1D, 2D, quasi-2D and 3D chiral HOIPs[33,34,83]. Low-dimensional HOIPs contain a greater percentage of chiral organic ligands and, thus, should exhibit a higher degree of chirality. For example, decreasing values of the anisotropy factor g_{abs} were observed for quasi-2D perovskites, as the value of <*n*> (the average number of inorganic layers between the chiral organic ligands) increased[83]. To date, only a select group of chiral ligands has been employed with perovskites (FIG. 4a).

The first chiral HOIP, incorporating the enantiomeric ligand (*S*)-methylbenzylammonium (*S*-MBA, FIG. 4a) was reported in 2003 (REF.[33]), and the corresponding 2D chiral HOIP single crystal in 2006 (REF.[34]). Structurally, R(or S)-MBAPbX$_3$ (X = Cl, Br or I) exhibits 1D polymeric face-sharing structures, whereas (R(or S)-MBA)$_2$PbI$_4$ exhibits 2D corner-sharing layered structures[34] (FIG. 4b). These enantiomers exhibit essentially the same cell parameters with mirror configuration and belong to the same Sohncke space group of $P2_12_12_1$. Chiral HOIPs were then extended to a new chiral ligand, 1-cyclohexylethylammonium (CHEA)[99] (FIG. 4a).

A series of 1D chiral HOIPs emitting white light were reported; the emission was attributed to exciton self-trapping, owing to the quantum confinement in low-dimensional perovskites[35,100–102]. As a result of introducing R-3-ammoniopiperidin-1-ium (3APD, FIG. 4a) as the chiral source, (R-3APD)PbCl$_4$·H$_2$O exhibits tunable emission from blue to yellow under different excitation wavelengths, with a high colour rendering index of 93.9 (REF.[35]). Another chloride-based chiral HOIP with R or S-1-(1-naphthyl)ethylammonium (NEA) as the chiral ligand (FIG. 4a) was reported[103]; the resulting (R-NEA)$_2$Pb$_4$Cl$_{10}$·2DMF and (S-NEA)$_2$-Pb$_4$Cl$_{10}$·2DMF exhibit a 2D layered structure (DMF: N,N-dimethylformamide), and both enantiomers belong to the $P2_1$ Sohncke space group. Interestingly, coordination four, five and six were observed for Pb (II) atoms in these 2D chiral HOIPs[103]. Other 2D chiral hybrid organic–inorganic lead perovskites based on MPEA[48] (β-methylphenethylammonium, FIG. 4a) and CMBA[40] (1-(4-chlorophenyl)ethylammonium, FIG. 4a), were also reported recently; we discuss them in the sections on nonlinear chiroptical applications and on ferroelectrics.

Lead-free chiral HOIPs based on tin[104,105], bismuth[37], copper[106–108], manganese[41], cadmium[109] and cobalt[110] were also reported, but their chiroptoelectronic and chiro-spintronic properties have not yet been studied.

Post-synthetic chiral-ligand exchange. In post-synthetic chiral-ligand exchange[111], the original ligands are exchanged partially or fully with chiral ligands. Unlike direct synthesis, in which chiral ligands influence the crystal structure, the chirality in this case is due to chiral surface distortion of the nanocrystals (induced by the capped ligands), chiral patterning of the surface ligands or the chiral field effect[47,82,94].

a Circularly polarized photodetector

b Circularly polarized light source

c Non-volatile memory

d Bioresponsive imaging

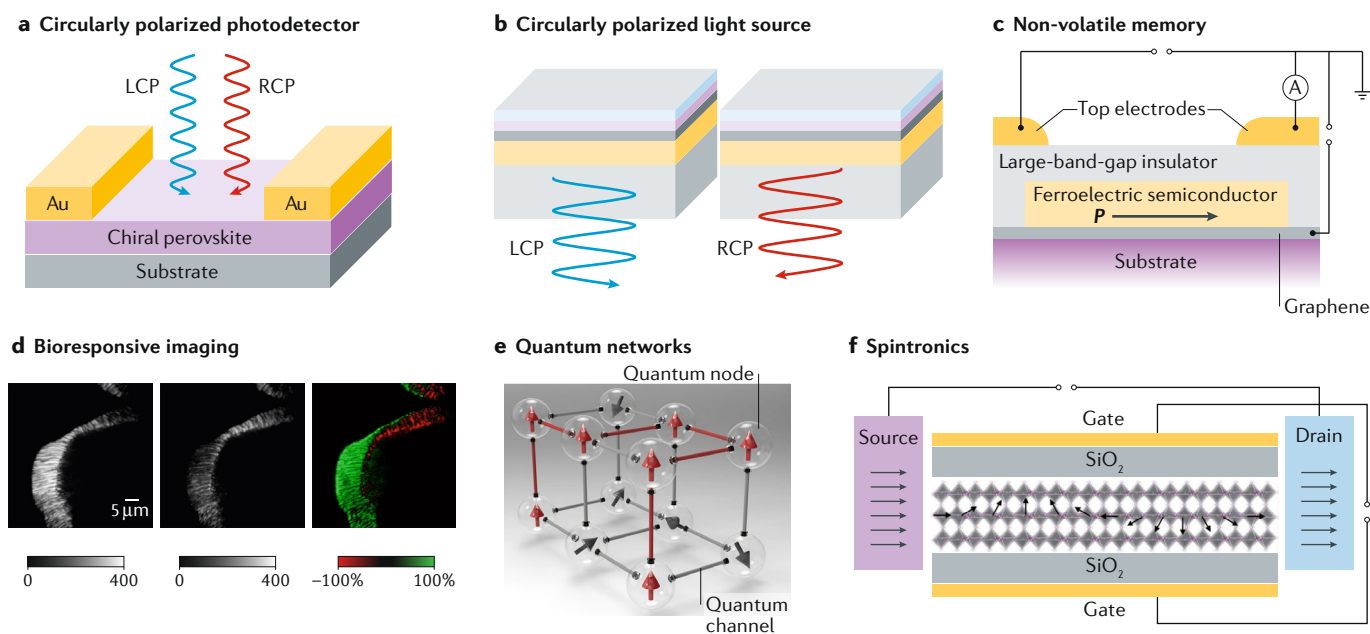**e** Quantum networks

f Spintronics

Fig. 1 | **Potential applications of chiral materials. a** | Circularly polarized photodetectors distinguish left-handed and right-handed circularly polarized (LCP and RCP, respectively) light. **b** | Circularly polarized light sources can emit LCP or RCP light. **c** | Non-volatile-memory devices can be built based on ferroelectric chiral materials with in-plane polarization P. **d** | In bioresponsive imaging, biological tissues respond differently to LCP and RCP excitations. The images shows, from left to right, second-harmonic generation (SHG) images of a ligament excited by LCP light, RCP light and the SHG circular dichroism image (Eq. 4). Compared with traditional SHG, polarization-resolved SHG exhibits higher contrast, which is beneficial towards imaging applications and provides more information on the collagen molecular properties. **e** | In quantum networks, spins are used as qubits in each node and photons are used as connections to build the quantum network. Chiral materials can be used as transducers between the spin and quantum states of light at each node of a quantum network. **f** | Spin field-effect transistor based on chiral perovskites. The spin precession from source to drain is controlled by the gate voltage. Owing to strong spin–orbit coupling in perovskites, chirality is strongly correlated with spin; thus, chiral perovskites can be used as spin current injectors and spin filters. Panel **b** is reproduced with permission from REF.[59], Wiley-VCH. Panel **c** is reproduced with permission from REF.[71], AAAS. Panel **d** is reproduced with permission from REF.[63], OSA Publishing. Panel **f** is reproduced with permission from REF.[72], ACS.

Chiral-perovskite nanocrystals (R-DACH nanocrystals and S-DACH nanocrystals) were obtained by replacing the oleylamine ligands with a small amount of chiral (1R, 2R)-1,2-diaminocyclohexane (R-DACH) or (1S, 2S)-1,2-diaminocyclohexane (S-DACH) ligands[79] (FIG. 5a). These chiral nanocrystals exhibit no circular dichroism signal from the region of the first excitonic transition band of the nanocrystal core (~580 nm). However, they do exhibit circular dichroism from 240 nm to 540 nm, owing to their chiral surface distortion and electronic interactions with the DACH ligands[79]. The photoluminescence of the perovskite nanocrystals is completely quenched by the chiral ligands.

Chiral-ligand-assisted reprecipitation method. In chiral-ligand-assisted reprecipitation, the ligands imprint chirality onto the electronic states of the quantum-confined perovskite. For instance, chirality was achieved in $CH_3NH_3PbBr_3$ perovskite nanoplatelets via chiral-ligand-assisted reprecipitation using R(or S)-MBA at room temperature[82]. The resulting circular dichroism spectra feature two regions: one arising from excitonic transitions of the perovskite (400–450 nm) and the other from charge-transfer transitions between the ligands and the nanoplatelets[82].

Chiral-ligand-assisted tip-sonication method. Recently, a simple, scalable, single-step and polar-solvent-free method to synthesize high-quality perovskite nanocrystals was developed: direct tip sonication[112]. Through the replacement of the achiral organic capping ligands on the surface of the nanocrystal with chiral molecules, chiral-perovskite nanocrystals could also be obtained. For example, R(or S)-α-octylamine (FIG. 4a) was employed as the chiral ligand[80]. In this case, the chirality of the perovskite nanocrystals originates from the surface distortion induced by the chiral ligands (FIG. 5b).

Chirality through environment
Chirality can also be induced in achiral molecular systems by tuning the environmental conditions by using chiral solvents[113], external stimuli (such as strain)[114], self-assembly on chiral templated structures like DNA[115], a chiral bias inducing chiral amplification into a supramolecular helical structure[116] and photoinduced inversion of helical chirality[117].

Whereas chiral molecules are recognized via their stereogenic centres, helical structures possess a chiral axis about which molecules are spatially arranged to yield non-superimposable mirror images[118]. 1D M and P chiral descriptors characterize left-handed and right-handed helices.

Helical chirality. A series of helical 1D chiral perovskites were synthesized through the introduction of achiral Schiff base cations, (*E*)-1-((3-Rbenzylidene)amino) pyridin-1-ium (*m*-RBz-1-APy$^+$; R = NO$_2$, Br, Cl or F)[119] (FIG. 5c). Two types of highly polarized 1D [PbI$_3$]$_\infty$ chains are coupled to the achiral organic cations by Coulomb and van der Waals forces, and the organic cations adopt a kagome-like tubular architecture (FIG. 5d). The obtained crystals are all in the same Sohncke space group of *P*6$_3$ (point group: *C*$_6$), enabling ferroelectricity[87,88]. A dielectric hysteresis loop was observed in these chiral perovskites, with a saturated polarization of 48 μC cm^{-2} at room temperature[119].

Another series of helical chiral perovskites were reported by using disulfide H$_3$N(CH$_2$)$_2$SS(CH$_2$)$_2$NH$_3$ ligands (a vital unit in biosystems) through solvothermal reaction[36]. The obtained α-[H$_3$N(CH$_2$)$_2$SS(CH$_2$)$_2$NH$_3$P-bI$_5$]·H$_2$O crystallizes into the *P*2$_1$ Sohncke space group, which displays an *M* helicity (left-handed helical form), opposite to that of the right-handed helical DNA. When α-[H$_3$N(CH$_2$)$_2$SS(CH$_2$)$_2$NH$_3$PbI$_5$]·H$_2$O is heated to 75 °C, a phase transition (conformation change) occurs from helical α-phase to the achiral racemic β-phase[36].

Supramolecular chiral-induction approach. When an achiral perovskite is incorporated into a chiral cogel, this induces chirality into the perovskite, as the achiral-perovskite nanocrystals follow the chirality of the gel structure to produce a chiral packing through supramolecular coassembly. Chiral-perovskite cogels were formed by dispersing perovskite nanocrystals into chiral lipid *N*,*N'*-bis(octadecyl)-L-glutamic diamide (LGAm) or its enantiomer *N*,*N'*-bis(octadecyl)-D-glutamic diamide (DGAm)[81] (FIG. 5e). Owing to the strong scattering from the gels, no obvious circular dichroism

signal was observed in the gel states; however, different handedness of induced circularly polarized photoluminescence (CPPL) was observed in the chiral cogels. The degree of photoluminescence polarization reached 0.365% at room temperature for CsPbBr$_3$ nanocrystals in DGAm, comparable to the value of 0.33% for CsPbBr$_3$ nanocrystals in LGAm. The CPPL could only be observed in the assembled state and disappeared in the disassembled state, which could be obtained through heating or using a polar solvent, such as chlorobenzene[81] (FIG. 5e).

Areas for improvement

For successful applications, the design of chiral perovskites must continue to advance. As discussed above, chirality has been introduced into perovskites via different strategies, each with their own advantages and disadvantages. Owing to their periodic nature, chiral-perovskite single crystals exhibit stronger chirality than polycrystals and thin films. Thus, future studies will benefit from improving film quality.

Helical chiral perovskites can be obtained starting from achiral ligands[36,119]; however, their prediction and design are difficult. Symmetry analysis reveals that reported chiral-perovskite single crystals have only a twofold rotation or twofold screw axis[33–37]. It is expected that structures incorporating higher-order symmetry operations will have stronger chirality. Theoretical modelling will aid in this effort.

Chiral-perovskite nanocrystals offer solution stability with colloidal states. Unfortunately, although different approaches have been employed to synthesize them, their chirality is generally low. Incorporation of a chiral matrix could be an effective strategy to overcome this issue. In principle, if the absorption and emission of perovskite nanocrystals overlap with the circularly polarized absorption (or transmittance) of the chiral matrix, stronger circularly polarized absorption and emission can be expected[120].

Chiroptoelectronic and ferroelectric applications

The chiroptical behaviour of 2D chiral (*R*-MBA)$_2$PbI$_4$ and (*S*-MBA)$_2$PbI$_4$ films has been explored in 2017 (REF.[47]). Strong, circularly polarized transitions flank the excitonic peak, showing that chiral perovskites exhibit the Cotton effect[121] (BOX 1). Circular differential scattering was also observed in the circular dichroism as the film thickness was increased[47]. However, when (*R*-MBA)$_2$PbI$_4$ or (*S*-MBA)$_2$PbI$_4$ powder was mixed with KBr to form a pellet, no obvious circular dichroism peaks were observed; this indicates that crystal orientation and crystallinity play a vital role in the total chirality of amorphous and polycrystalline chiral-perovskite samples[47].

Circularly polarized photodetectors

Left-handed and right-handed CPL can be used as two independent channels to transmit information, doubling the rate of data transport compared with unpolarized light[122]. The development of CPL-based communication requires high-performance circularly polarized photodetectors and CPL sources. Unlike indirect methods of detecting and emitting CPL, chiral materials do not
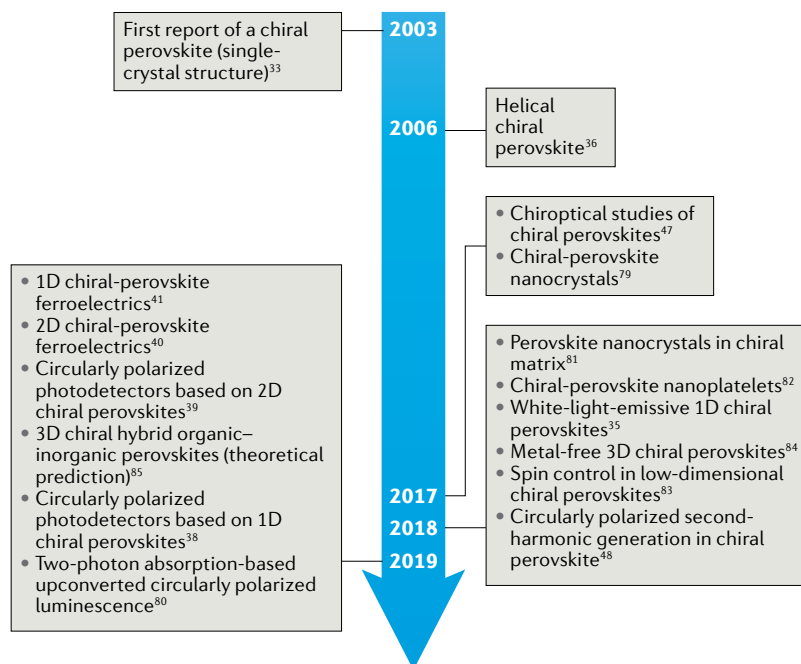

Fig. 2 | Timeline of research on chiral perovskites. Timeline showing key events in the development of chiral perovskites.
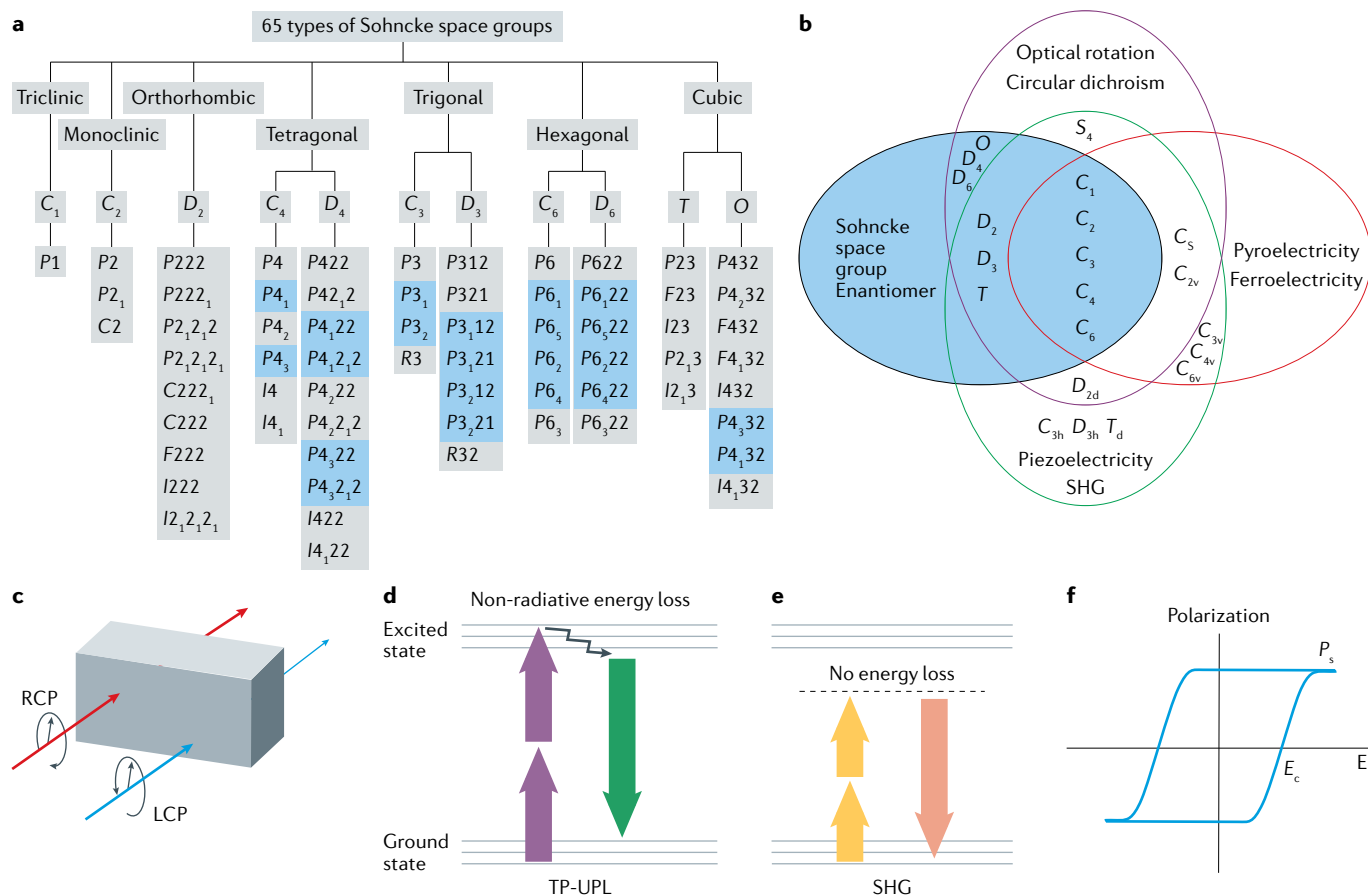
Timeline entries:

- **2003** — First report of a chiral perovskite (single-crystal structure)[33]
- **2006** — Helical chiral perovskite[36]
- Chiroptical studies of chiral perovskites[47]
- Chiral-perovskite nanocrystals[79]
- 1D chiral-perovskite ferroelectrics[41]
- 2D chiral-perovskite ferroelectrics[40]
- Circularly polarized photodetectors based on 2D chiral perovskites[39]
- 3D chiral hybrid organic–inorganic perovskites (theoretical prediction)[85]
- Circularly polarized photodetectors based on 1D chiral perovskites[38]
- Two-photon absorption-based upconverted circularly polarized luminescence[80]
- **2017 / 2018 / 2019** — Perovskite nanocrystals in chiral matrix[81]; Chiral-perovskite nanoplatelets[82]; White-light-emissive 1D chiral perovskites[35]; Metal-free 3D chiral perovskites[84]; Spin control in low-dimensional chiral perovskites[83]; Circularly polarized second-harmonic generation in chiral perovskite[48]

Fig. 3 | **Basics of chiral-material properties. a** | There are 65 types of Sohncke space groups within different Bravais lattices and point groups. Chiral space groups are highlighted in blue; crystal structures belonging to the 65 listed Sohncke space groups are chiral. **b** | The Neumann–Curie principle determines the structure–property relationship of non-centrosymmetric crystals. **c** | Circular dichroism is a phenomenon whereby a material absorbs more of one circular polarized light than the other (in this example, left-handed circularly polarized (LCP) rather than right-handed circularly polarized (RCP) light). **d** | Schematic representation of two-photon absorption-based upconverted photoluminescence (TP-UPL). **e** | Schematic representation of second-harmonic generation (SHG) processes. **f** | Ferroelectric polarization versus electrical field E hysteresis loop for ferroelectric materials; the saturated polarization (P_s) and coercivity (E_c) are marked. Panel **b** is reproduced with permission from REF.[133], ACS.

require additional optics; thus, circularly polarized photodetectors and light sources based on chiral materials are promising for integrated and flexible devices.

HOIPs have been demonstrated as effective photodetectors owing to their low trap density[1], strong light sensitivity[23,24] and tunable absorptions[14]. Similarly, by combining the impressive optical and electrical properties of HOIPs with chirality, chiral HOIPs should be promising for the detection of CPL[38,39]. Currently, there are only a few reports on direct CPL detection from different material systems[52–55]. A major challenge for CPL photodetectors is combining chirality (usually associated with organic molecules) and efficient charge transport (usually associated with inorganic semiconductors). Therefore, chiral HOIPs are especially promising, as they benefit from both aspects[38,39].

Recently, a CPL photodetector based on 1D chiral perovskites was reported[38] (FIG. 6a). 1D chiral perovskites have the largest molar ratio of chiral ligands compared with 2D and quasi-2D chiral perovskites, and, thus, should exhibit the strongest CPL response. A relationship

between the thickness of the chiral medium and its ability to distinguish left-handed circularly polarized (LCP) and right-handed circularly polarized (RCP) light ($\Delta c/c$) for photoconductive CPL detection was formulated as:

$$\frac{\Delta c}{c} = \frac{c_L - c_R}{(c_L + c_R)/2} \approx \frac{\Delta\alpha \cdot d}{\exp(\alpha_L d) - 1} \tag{1}$$

where Δc is the difference between the carrier concentration generated by LCP and RCP light illumination ($\Delta c = c_L - c_R$), whereas c is the average carrier concentration ($c = (c_L + c_R)/2$), $\Delta\alpha$ is the difference between the absorption coefficients for LCP (α_L) and RCP (α_R) light and d is the thickness of the chiral medium. Increasing the thickness of the chiral medium results in a decrease of the CPL response (FIG. 6b). Thus, an optimal thickness of the chiral HOIPs film is necessary to achieve the most efficient CPL photodetection.

At a low CPL intensity of $5\,\mu W\,cm^{-2}$ (395 nm), the responsivity reaches $120\,mA\,W^{-1}$ (FIG. 6c), which is almost two orders of magnitude larger than the CPL

Box 1 | **Key terms**

Sohncke space groups
The Sohncke space groups are the 3D space groups containing only operations of the first kind (rotations, roto-translations, translations). Among the 230 types of space groups, 65 are Sohncke[86,182] (FIG. 3a). If a material's crystal structure belongs to a Sohncke space group, then that material is chiral.

Neumann–Curie principle
The Neumann–Curie principle defines the relationship between Sohncke space groups and the corresponding properties, such as circular dichroism, second-harmonic generation (SHG) and ferroelectricity[87,88] (FIG. 3b). For instance, all chiral single crystals exhibit optical rotation and circular dichroism. However, optical rotation and circular dichroism can also be observed in non-centrosymmetric achiral point groups, such as S_4, C_s, C_{2v} and D_{2d}. Similarly, most of the Sohncke groups are SHG active, but not those in the point groups O, D_4 and D_6.

Circular dichroism
Circular dichroism is a phenomenon whereby a material absorbs more of one circular polarization than the other, making the transmitted light elliptical[46] (FIG. 3c). The degree of chirality can be represented in terms of ellipticity (θ, in mdeg)[183] or anisotropy factor (g_{abs})[184].

Ellipticity
The ellipticity (θ, in mdeg) is calculated based on the equation:

$$\theta \ (mdeg) = \Delta A \left(\frac{\ln 10}{4} \right) \left(\frac{180000}{\pi} \right) \tag{5}$$

where ΔA is the difference in absorption of the left-handed (A_L) versus right-handed (A_R) circularly polarized light.

Anisotropy factor
The anisotropy factor[184] is the ratio of circular dichroism to conventional absorption, defined by:

$$g_{abs} = \frac{A_L - A_R}{(A_L + A_R)/2} \tag{6}$$

In this scale, the values range from −2 (absorbing only right-handed circularly polarized (RCP) light) to 2 (absorbing only left-handed circularly polarized (LCP) light), with 0 indicating the absorption of both equally.

Circularly polarized photoluminescence
Circularly polarized photoluminescence (CPPL) results from different emission strengths of LCP versus RCP light. The degree of photoluminescence polarization (DP) is given by:

$$DP = \frac{I_L - I_R}{I_L + I_R} \tag{7}$$

where I_L and I_R are the emission intensities of LCP and RCP light, respectively. Values of DP close to −1 or 1 indicate pure RCP or LCP photoluminescence, respectively, whereas a value of 0 indicates no CPPL.

Cotton effect
The Cotton effect shifts absorption spectra for LCP versus RCP light, resulting in the characteristic dispersive feature in circular-dichroism spectroscopy.

Two-photon absorption-based upconverted photoluminescence
Two-photon absorption-based upconverted photoluminescence (TP-UPL) occurs when a fluorophore absorbs two photons whose combined energy equals that of the electronic transition. Fluorescence resulting from this process occurs at a higher energy than that of the incoming photons (upconverted fluorescence, FIG. 3d).

Second-harmonic generation
SHG, also called frequency doubling, is a nonlinear optical process in which two photons interact with a nonlinear material to effectively combine to form new photons with twice the frequency of the initial photons[185] (FIG. 3e).

Ferroelectricity
Ferroelectric materials have intrinsic spontaneous electric polarization, even in the absence of an applied electric field (FIG. 3f). Ferroelectric materials are described using the saturated polarization[186] and coercivity[91]. The saturated polarization is the largest ferroelectric polarization that the material achieves under an external electric field, whereas coercivity is the minimum electric field required to depolarize a ferroelectric material after it has been driven to saturation.

photodetectors based on plasmonic silver metamaterials[53]. The distinguishability (g_{res}) of these chiral-perovskite-based circularly polarized photodetectors is calculated as:

$$g_{res} = \frac{2(R_L - R_R)}{R_L + R_R} \tag{2}$$

where R_L and R_R are the responsivities of the circularly polarized photodetector under LCP and RCP light illumination, respectively. Similar to g_{abs}, g_{res} also ranges from −2 to 2, which stand for pure LCP or RCP light detection, respectively, whereas 0 indicates no distinguishability between LCP and RCP light. Here, for this 1D chiral-perovskite-based CPL photodetector, the

measured g_{res} is 0.10 at 395 nm, higher than the anisotropy factor of 0.02 obtained from circular dichroism measurements (FIG. 6c); this discrepancy was attributed to the spin-dependent carrier generation[27], transport and collection[123] for chiral perovskites under CPL excitation. The performance of these 1D chiral-perovskite-based CPL photodetectors remained almost the same after one month under ambient conditions without encapsulation. A flexible CPL photodetector was also fabricated on a polyethylene terephthalate substrate, and the performance exhibited negligible degradation upon 100 cycles of bending[38].

A CPL photodetector based on 2D chiral perovskite/MoS_2 heterojunctions was also reported[39]. The device reached a responsivity of 450 mA W^{-1} at 519 nm and a detectivity of 2.2×10^{11} Jones[39]. The calculated g_{res} was 0.09 at 510 nm (FIG. 6d), similar to that of CPL photodetectors based on 1D chiral perovskites.

At this stage, the performance of CPL photodetectors is still far from that required for practical applications. In-depth work is still needed to increase the anisotropy factor (g_{res}) of chiral-perovskite materials (see Section 2 of the Supplementary Information). As outlined earlier, different strategies (such as better crystallinity, higher-order rotation/screw symmetry, chiral perovskites in chiral matrices) may prove effective to this end.

Circularly polarized light sources

In addition to data transfer, CPL sources have applications in bioresponsive imaging[61,62], 3D displays[64,65], anti-counterfeiting[124], quantum computing[66,67] and spintronics[43,44]. For example, light polarization is very important for high-contrast and efficient displays. To eliminate the glare from external light sources (such as sunlight), circularly polarized anti-glare filters are widely used to trap ambient light in the display. However, if the light source is unpolarized, roughly half of the emitted light is blocked by the anti-glare filters, substantially decreasing its brightness and efficiency. Chiral materials are promising because they produce CPL that can be transmitted unimpeded through the filters[54,60,125]. Recently, circularly polarized LEDs with degrees of electroluminescence polarization over 50% were reported[73,74].

HOIPs have been demonstrated as efficient LEDs, with external quantum efficiencies reaching over 20%[12,126,127]. Therefore, chiral HOIPs are promising candidates for CPL sources. However, 2D chiral-perovskite films generally exhibit poor photoluminescence quantum yields (PLQYs) at room temperature, owing to strong, non-radiative recombination[128]. To overcome this issue, low-dimensional chiral perovskites (LDCPs) were developed (FIG. 7a). Through combined strategies of energy funnelling[10,11] and chirality transfer[92,93], efficient emission was enabled while maintaining the intrinsic optical, electrical and spintronic properties of the perovskites[83]. Both circular dichroism and CPPL were observed in these LDCPs. They exhibited a PLQY of 90% due to strong energy funnelling and a 3% CPPL was observed in the absence of an external magnetic field[83] (FIG. 7b–d). For comparison, 3D achiral perovskites can only achieve a comparable degree of photoluminescence polarization under an external magnetic field of 5 T (REF.[129]).

The photoluminescence polarization of LDCPs arises from asymmetric emission rates of LCP and RCP light based on Einstein coefficients[130]. In two-level systems, Einstein coefficients relate the absorption rate to the emission rate. Because the emission of LDCPs only originates from one excited state (the component with higher $<n>$) decaying to the ground state, the system is effectively a two-level system. Hence, an asymmetric absorption rate (circular dichroism) between spin up and spin down implies an asymmetric emission rate between the two spin species. The degree of photoluminescence polarization can be tuned further through the Zeeman interaction by applying an external magnetic field. For R-LDCP, when a positive magnetic field is applied, the contribution by the intrinsic asymmetric emission rates and Zeeman interaction are synergistic. Therefore, the photoluminescence polarization increases when applying a positive magnetic field (FIG. 7c, range I). However, when a negative magnetic field is applied, there

Table 1 | **Chirality-transfer mechanisms, dimensionality, form and applications of chiral perovskites**

Chemical formula	Mechanism	Dimensionality	Form	Application
(R-MBA)$_2$PbI$_4$ (REFS[34,39])	I	2D	Microplates	CPL source
(R-CMBA)$_2$PbI$_4$ (REF.[40])	I	2D	Crystal	Ferroelectric
R-3-FP-MnCl$_3$ (REF.[41])	I	1D	Crystal	Ferroelectric
(R-MPEA)$_{1.5}$PbBr$_{3.5}$(DMSO)$_{0.5}$ (REF.[48])	I	2D	Crystal	NLO, CP-SHG
(R-3APD)PbCl$_4$·H$_2$O (REF.[35])	I	1D	Crystal	White-light source
R-MBAPbI$_3$ (REF.[38])	II	1D	Film	CPL photodetector
R-LDCP[83]	II	Quasi-2D	Film	Spintronics
R-Pero-NCs[80]	II	0D	Colloidal nanocrystal	NLO, TP-UCPPL
R-DACH-NCs[79]	II	0D	Colloidal nanocrystal	CPL photodetector
Pero-NCs (DGAm)[81]	II	0D	Chiral cogel	CPL source
R-MBA-NPs[82]	IV	0D	Colloidal nanoplatelets	CPL photodetector

Mechanisms: I, ligand-induced chiral inorganic structure; II, chiral distortion of the inorganic surface; III, chiral patterning of the surface ligands; IV, chiral field effect. CPL, circularly polarized light; CP-SHG: circularly polarized second-harmonic generation; DMSO; dimethyl sulfoxide; NCs, nanocrystals; NLO, nonlinear optics; TP-UCPPL, two-photon absorption-based upconverted circularly polarized photoluminescence.
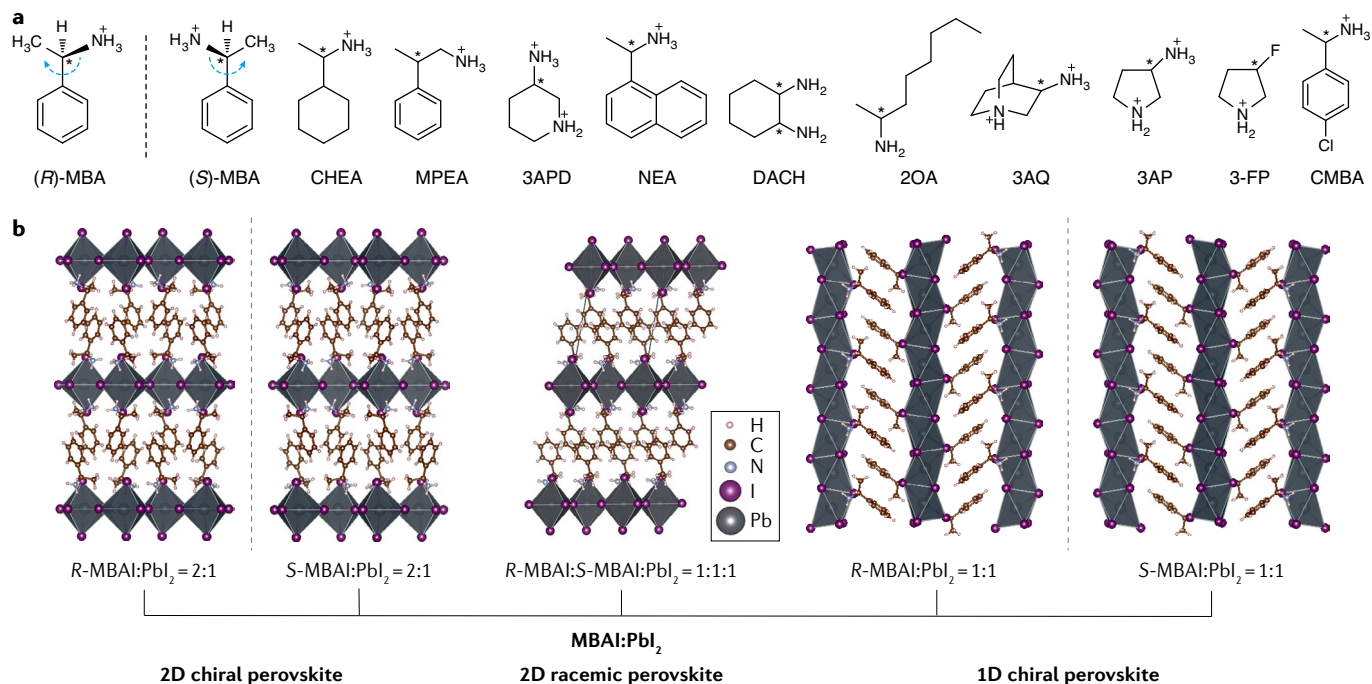
a

(R)-MBA   (S)-MBA   CHEA   MPEA   3APD   NEA   DACH   2OA   3AQ   3AP   3-FP   CMBA

b

H	○
C	●
N	○
I	●
Pb	●

R-MBAI₂:PbI₂ = 2:1   S-MBAI₂:PbI₂ = 2:1   R-MBAI:S-MBAI:PbI₂ = 1:1:1   R-MBAI:PbI₂ = 1:1   S-MBAI:PbI₂ = 1:1

MBAI:PbI₂

2D chiral perovskite   2D racemic perovskite   1D chiral perovskite

Fig. 4 | **Representative chiral ligands and chiral hybrid organic–inorganic perovskites. a** | The chiral ligands discussed in this Review: MBA (methylbenzylammonium), CHEA (1-cyclohexylethylammonium), MPEA (β-methylphenethylammonium), 3APD (R-3-aminopiperidine), NEA (1-(1-naphthyl)ethylammonium), DACH (1,2-diaminocyclohexane), 2OA (2-octylamine), 3AQ (3-ammonioquinuclidinium), 3AP (3-ammoniopyrrolidinium), 3-FP (3-fluoropyrrolidinium) and CMBA (1-(4-chlorophenyl)-ethylammonium). Based on the Cahn–Ingold–Prelog priority rules, the four groups around a chiral centre are prioritized according to the atomic number and priority. This begins with the four atoms closest to the chiral centre and moves to subsequent atoms in the event of a tie. With the fourth (the lowest priority) group facing away from the viewer, a path can be traced from groups 1–2–3. If this path is clockwise, the chiral centre is designated as R (from the Latin word 'rectus'); conversely, if it is anticlockwise, the chiral centre is designated as S (from the Latin word 'sinister'). The clockwise and anticlockwise directions are shown (blue arrows) according to the priority of the four groups. **b** | Single-crystal structures of 2D and 1D chiral perovskites and of a 2D racemic achiral perovskite based on MBA: (R-MBA)₂PbI₄, (S-MBA)₂PbI₄, R-MBAPbI₃, S-MBAPbI₃ and (rac-MBA)₂PbI₄.

is a competition between the intrinsic asymmetric emission rates and the Zeeman interaction (FIG. 7c, ranges II and III). The photoluminescence polarization decreases to zero when the negative magnetic field reaches −2.8 T, where the contribution by intrinsic asymmetric emission rates balances the Zeeman splitting. Further increasing the negative magnetic field allows the Zeeman interaction to play the leading role, and the photoluminescence polarization becomes negative[83] (FIG. 7c, range III). The magnetic-field dependence in these chiral perovskites (FIG. 7b–d) is fitted as:

$$DP = \frac{g_{eff}\mu_B B}{k_B T} + DP_0 \tag{3}$$

where g_{eff} is the effective g factor of the spin-1/2 electron and hole in the spin-pair species, μ_B is the Bohr magneton, B is the applied magnetic field, DP_0 is the degree of polarization introduced by the chirality in the absence of the magnetic field, k_B is the Boltzmann constant and T is the temperature. Based on the fitting results, the g_{eff} for R-LDCPs, S-LDCPs and rac-LDCPs are, respectively, 0.032, 0.031 and 0.027.

The influence of temperature on the photoluminescence polarization of pure 2D chiral (R-MBA)₂PbI₄ and (S-MBA)₂PbI₄ microplates has also been systematically investigated[39]. A record photoluminescence polarization of 17.3% was observed at 77 K (REF.[39]). With increasing temperature, the degree of photoluminescence polarization decreases substantially due to the enhanced electron–phonon couplings and thermal-expansion interactions, which reduce the lattice distortion and, thus, decrease the chirality[39]. In addition, increased temperature also results in spin mixing, which further decreases the degree of polarization[129].

At this stage, most studies on CPL sources with chiral HOIPs have been performed at cryogenic temperatures. For practical application, future work should focus on achieving high photoluminescence polarization at elevated temperatures. This will require developing novel chiral-perovskite materials with strong chirality[39], as DP has been shown to decrease dramatically with increasing temperatures[129]. A better understanding of this correlation may also help to direct synthesis towards weakening or even eliminating this temperature dependence.

Nonlinear chiroptical effects

Nonlinear optics describes a large body of phenomena in which a medium behaves nonlinearly with respect to optical excitations (in terms of optical power). The magnitude of the nonlinearity gives a measure of medium-assisted light–light interaction in the material.

A strong nonlinear response is desirable in applications such as data processing, which use integrated photonic circuits for realizing higher data-transmission rates[131], or nonlinear microscopy, in which nonlinearity helps to obtain more information on the studied sample[132]. Nonlinear effects can be classified by their order or the number of interacting photons needed to describe the phenomena (for example, second-order nonlinear optics involve two-photon interactions). As a basic rule, the interaction becomes weaker as its order increases. Hence, the strongest nonlinear effects should be second order.

However, for even-order nonlinear optical responses like SHG, strict structural non-centrosymmetry is required[133]. A series of non-centrosymmetric achiral perovskites was reported recently, and SHG[134], two-photon absorption[135] and linear electro-optic effects[136] were observed. However, predicting or designing non-centrosymmetric achiral perovskites is challenging. Thus, the exploration of optical nonlinearities in perovskites has been focused mainly on the odd-order nonlinear optical effects[137,138]. Chiral HOIPs are intrinsically non-centrosymmetric and, thus, are promising for nonlinear chiroptical applications[48,80]. Additionally, because chiral HOIPs can couple to CPL, they can be utilized in chiral integrated photonic circuits[139–141], which have been shown to have higher efficiency than conventional circuits[142].

Nonlinear chiroptical effects were recently observed in 2D chiral HOIPs based on β-MPEA (FIG. 4a). A solvent-engineered chiral perovskite (FIG. 7e) was obtained by using an antisolvent-vapour-assisted crystallization strategy, in which dimethyl sulfoxide (DMSO) molecules axially coordinate with Pb^{2+} in the partially edge-shared octahedra in $(MPEA)_{1.5}PbBr_{3.5}(DMSO)_{0.5}$ (REF.[48]). Both circular dichroism and polarization-dependent SHG were observed in these chiral-perovskite nanowires.

Polarization-dependent SHG was observed under a circularly polarized excitation at 850 nm (FIG. 7f). The SHG circular dichroism (SHG-CD) is defined as:

$$SHG - CD = (I_{RCP} - I_{LCP})/(I_{RCP} + I_{LCP}) \qquad (4)$$

where I_{RCP} and I_{LCP} are the SHG intensity under RCP and LCP excitation, respectively. Vertical and horizontal analysers are used to analyse the polarization of the generated SHG signal. If the SHG signal is only due to the circular dichroism, the intensity is the same for the vertical and horizontal analysers. In $(R\text{-}MPEA)_{1.5}PbBr_{3.5}(DMSO)_{0.5}$ nanowires, the SHG-CD reaches a large value, indicating promising future towards nonlinear chiroptical applications[48].

Beyond second-order nonlinear effects, one important nonlinear chiroptical effect is two-photon absorption-based upconverted circularly polarized photoluminescence (TP-UCPPL), which has recently been observed in chiral-perovskite nanocrystals[80]. Unlike traditional one-photon absorption CPPL, TP-UCPPL doubles the excitation wavelength. The CPPL of chiral-perovskite nanocrystals in a poly(methyl methacrylate) matrix was measured and the results indicated that two-photon and one-photon circularly polarized excitations give a similar degree of photoluminescence polarization, around 0.25%[80]. Therefore, TP-UCPPL can replace one-photon absorption CPPL if the doubled wavelength is more suited for a specific application. Such applications include imaging of biosystems (where red or near-infrared light is needed to penetrate the skin)[143,144] and chiroptoelectronics (as telecommunications use near-infrared bands)[122].

Future work on nonlinear chiroptical effects should focus on determining the correlation between space group and efficiency in SHG and TP-UCPPL. Because non-centrosymmetry is required, it will be important to learn which space group provides the strongest nonlinear chiroptical effects. From there, a more directed approach will be available to improve performance. Furthermore, the optimization of the phase-matching condition (between the SHG signal and the excitation signal), working temperature and dimensionality are important for SHG. The phase-matching condition has a pronounced effect on the generated second-harmonic power[145]. Likewise, temperature and dimensionality can affect the value of the second-order susceptibility[139]. Hence, optimization of all these parameters is necessary for practical application of second-order nonlinear chiroptics.

Ferroelectric properties

Ferroelectric materials are a class of functional materials that are widely used in electrocaloric devices, ferroelectric random-access memories and dynamic random-access memory capacitors[146,147]. Based on the Neumann–Curie principle[87,88], chiral perovskites are expected to exhibit intrinsic ferroelectric properties if they crystallize in the special point groups of C_1, C_2, C_3, C_4 and C_6. Owing to the organic and inorganic hybrid nature, the ferroelectric performance of chiral perovskites can be tuned efficiently through rational design of chiral organic ligands and the introduction of different metals[40,41,84,109].

Recently, a series of ferroelectric chiral perovskites, ranging from 3D metal-free chiral perovskites[84] to 1D chiral hybrid organic–inorganic manganese perovskites[41] and 2D chiral hybrid organic–inorganic lead perovskites[40], were reported. In 3D metal-free chiral perovskites[84] (FIG. 8a), chiral 3-ammoniopyrrolidinium (3AP, FIG. 4a) and 3-ammonioquinuclidinium (3AQ, FIG. 4a) were employed to introduce chirality, and the resulting R(or S)-3AP-NH$_4$X$_3$ and R(or S)-3AQ-NH$_4$X$_3$ belong to the $P2_1$ Sohncke space group at room temperature (X = Cl or Br), thus enabling pyroelectric and ferroelectric properties[87,88].

Later, different halide atoms were introduced to obtain 1D and 2D chiral HOIPs[40,41]. Owing to the strong electron-withdrawing ability of fluorine and chlorine atoms, the electric dipole moment was enhanced, thus, increasing the saturated polarization under an electric field. Moreover, the intermolecular interactions could be enhanced through hydrogen bonds and dipole–dipole interactions; thus, the ferroelectric working temperature could be increased to above room temperature.

For example, the introduction of fluorine atoms into (pyrrolidinium)MnCl$_3$ (REF.[148]) increased the phase-transition temperature for the obtained chiral
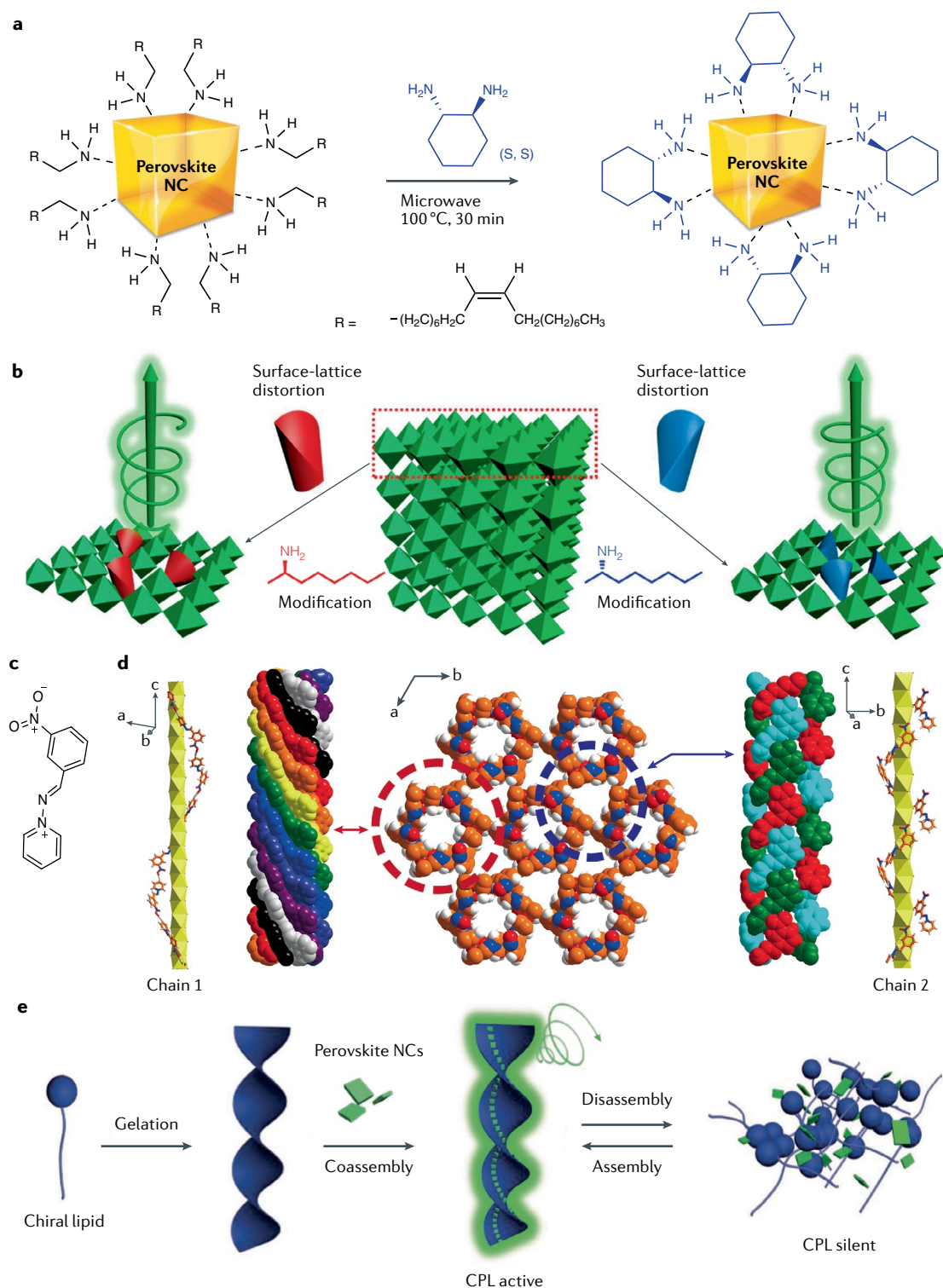
R(and S)-3-FP-MnCl₃ (3-FP, FIG. 4a) to 333 K (REF.[41]), compared with 295 K for the parent compound (pyrrolidinium)MnCl₃. The saturated polarization of R-3-FP-MnCl₃ and S-3-FP-MnCl₃ reaches 5.0 and 5.4 μC cm⁻² at 313 K, respectively, and decreases to zero after heating to the paraelectric phase at 363 K (REF.[41]) (FIG. 8b,c). Recently, this strategy was extended to 1D hybrid organic–inorganic cadmium chiral perovskites[109]: the phase-transition temperature increased by 63 K after introducing fluorine, while the saturated polarization increased from 3.6 to 5.79 μC cm⁻².

Chlorine, another electron-withdrawing atom, was introduced to the para position of MBA (CMBA, FIG. 4a), and 2D chiral (R-CMBA)₂PbI₄ and (S-CMBA)₂PbI₄ were obtained[40] (FIG. 8d). The incorporation of the chlorine atom decreases the crystal symmetry from the highly symmetric P2₁2₁2₁ space group of (R-MBA)₂PbI₄ (REF.[34]) to the lower-symmetry space group P1 for

◀ Fig. 5 | **Chirality through chiral ligands and environment. a** | Post-synthetic chiral-ligand-exchange strategy to synthesize chiral-perovskite nanocrystals (NCs). **b** | Schematic illustration of the use of the chiral-ligand-assisted tip-sonication method to prepare chiral-perovskite NCs. Through adding the chiral ligands (left: *R*-2-octylamine, right: *S*-2-octylamine) during the direct tip-sonication process, chirality is introduced into the perovskite NC through surface-lattice distortion by the chiral ligands. **c** | The molecular structure of the achiral Schiff base cation: (*E*)-1-((3-nitrobenzylidene)amino)pyridin-1-ium. **d** | The achiral (*E*)-1-((3-nitrobenzylidene)amino)pyridin-1-ium cations adopt a kagome-like tubular architecture: nonuple-stranded helices around the highly polarized 1D $[PbI_3]_\infty$ chains (chain 1, sixfold screw axis) and triple-stranded helices around the highly polarized 1D $[PbI_3]_\infty$ chains (chain 2, C_3 rotation axis). **e** | In the supramolecular chiral-induction approach, achiral-perovskite NCs follow the chirality of a gel structure to produce a chiral cogel. These coassembled structures emit circularly polarized light (CPL); the CPL signal is switched via heating or cooling the cogel, as the disassembled state obtained by heating does not emit CPL. Panel **a** is reproduced with permission from REF.[79], AIP. Panel **b** is reproduced with permission from REF.[80], ACS. Panel **d** is reproduced with permission from REF.[119], ACS. Panel **e** is reproduced with permission from REF.[81], Wiley-VCH.

(*R*-CMBA)$_2$PbI$_4$; thus, (*R*-CMBA)$_2$PbI$_4$ exhibits intrinsic ferroelectricity, whereas (*R*-MBA)$_2$PbI$_4$ does not. Both (*R*-CMBA)$_2$PbI$_4$ and (*S*-CMBA)$_2$PbI$_4$ exhibit a large saturated polarization of 13.96 µC cm^{-2} at 293 K based on the point-charge model.

However, the above ferroelectric performances were measured on single crystals, not thin films. For commercial application, ferroelectric materials should be solution processed, which would enable integrated ferroelectric devices[146,147]. Thus, the next step is developing high-performance multiaxial ferroelectric films[149].

Outlook

Although chiral perovskites were first synthesized in the early 2000s[33], their chiroptical properties were only measured as recently as in 2017 (REF.[47]). Since then, reports of chiral perovskites have become more prevalent[35,37–41,48,79–85,109,150]. As this trend continues, we expect that more researchers will begin to explore their properties, new fields will open up and new applications will be targeted. Here, we discuss specific areas of interest for chiral perovskites.

3D chiral perovskites

Compared with their low-dimensional counterparts, 3D chiral HOIPs should have smaller exciton-binding energies and longer carrier-diffusion lengths, which should prove advantageous in chiroptoelectronic and spintronic applications. As of today, however, 3D chiral HOIPs have yet to be synthesized. Recently, theoretical calculations have shown that 3D chiral perovskites should be both thermodynamically and kinetically stable[85]. These 3D chiral perovskites would contain a chiral cation such as $CHFClNH_3^+$ or $CHDFNH_3^+$. Note that these two chiral cations are the simplest known practical forms of chiral ligands, although other varieties of small chiral ligands could also be possible[151]. If they can be synthesized, we believe that the resulting 3D chiral HOIPs will find wide applications, including the production of circularly polarized perovskite waveguides[152], photodetectors[38] and lasers[153], second-order nonlinear optical imaging[61], chiro-spintronics[43,44] and topological quantum engineering[51].

Spintronic applications

Recently, it was discovered that chiral molecules can be used in the injection and detection of spin signals[43], and the combination of the spin-filtering effect of molecular chirality and spintronics nurtures a new research domain, called chiro-spintronics or chiral-based spintronics[43,44].

Achiral perovskites recently showed promising spin-related properties[32], including strong spin–orbit coupling[129], large Rashba splitting[25,26,154] and long spin lifetimes[27–29]. However, they require the use of a magnetic field or a circularly polarized excitation to generate spin-polarized carriers, whereas chiral perovskites inherently enable spin-polarized absorption and emission. In addition, chiral perovskites provide a platform for spin transport[31] and spin manipulation[30,39,83]. Recently, optical spin manipulation was demonstrated in low-dimensional chiral perovskites in the absence of an external magnetic field[83]. Chiral perovskites exhibit asymmetric circular polarization emission rates[83], which leads to an imbalanced population of different spin species of charge carrier, even under continuous, unpolarized excitation. This could be utilized to create a spin current either in the perovskite itself or by spin injection into a ferromagnetic material. This is in contrast to the creation of a spin imbalance in achiral materials such as achiral perovskites or transition-metal dichalcogenide monolayers, where a circularly polarized excitation or an external magnetic field are required[30,129,155,156].

Another interesting way to view chirality transfer is treating it as a spintronic equivalent of doping in semiconducting electronics. Owing to the correlation between chirality and spin selectivity, we can 'dope' materials with different handedness of chirality through rational design. Hence, making a junction between two materials with different chirality could result in a spin diode; that is, a device that allows spin currents to flow only in one direction. It is straightforward to extend this view to a chiral-based spin transistor and, hence, a fully chiral-based spintronic circuit. Moreover, if the material is light emitting, such as chiral perovskites, this could result in spintronic photodiodes and LEDs, in which the detection of light results in a spin current, and the emission of light depends on a spin current. All these devices would work under zero magnetic field.

Chiral quantum devices

One advantage of spin-based devices over charge-based electronics is that Joule heating is minimized, resulting in more energy-efficient devices. In addition, spin (or, in general, angular momentum) represents an additional degree of freedom to carry information. Therefore, spin is one of the best candidates for the physical realization of quantum bits[66]. It has been noted that chirality may also play an important role in quantum communications[157].

For quantum communications, photon polarization is used for carrying quantum information in a variety of schemes. As such, a well-polarized and highly efficient single photon source is desired. For most well-established single-photon sources, such as InGaAs quantum dots, emission is unpolarized[158].
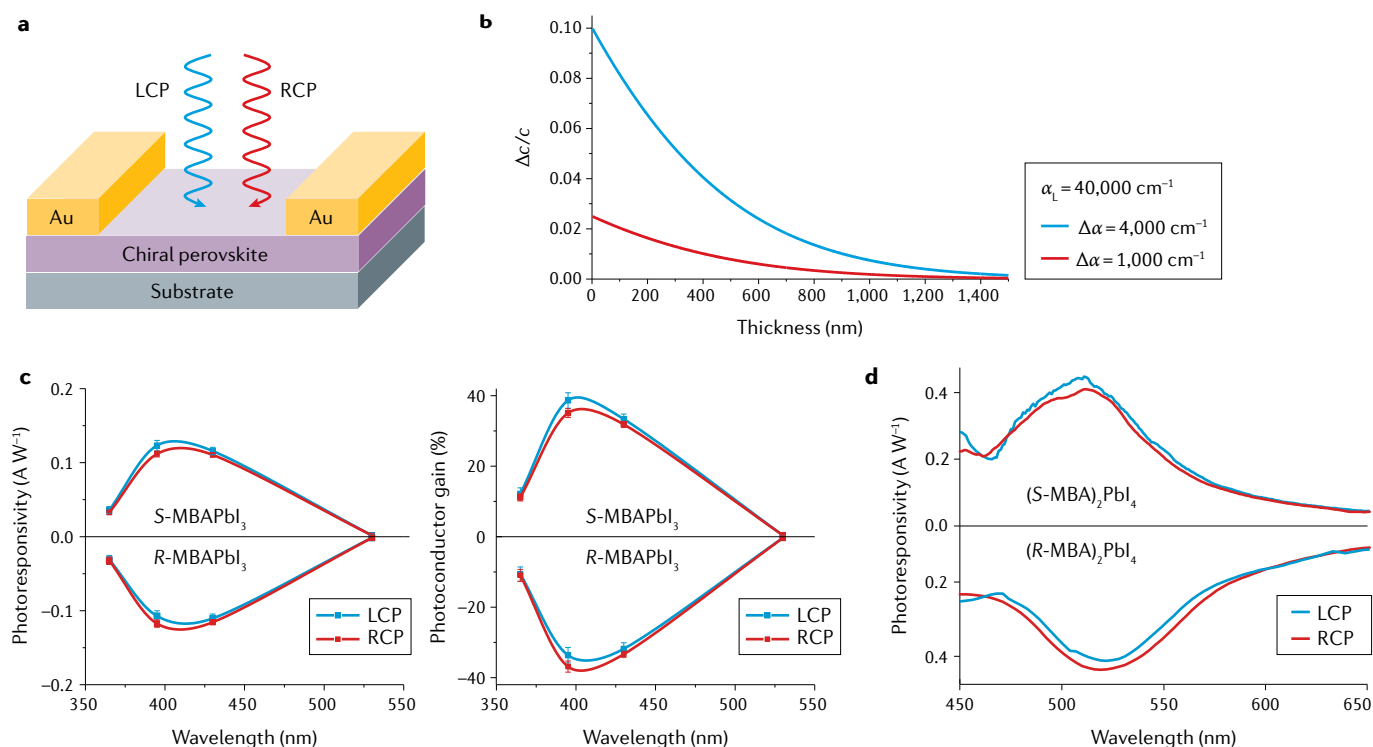
Fig. 6 | **Circularly polarized photodetectors based on chiral hybrid organic–inorganic perovskites. a** | Structure of a circularly polarized photodetector based on 1D chiral perovskites. **b** | The relationship between the thickness of the chiral medium and the ability to distinguish left-handed circularly polarized (LCP) and right-handed circularly polarized (RCP) light ($\Delta c/c$) for photoconductive circularly polarized light detection. Starting from an absorption coefficient of LCP light for a chiral medium of $\alpha_L = 40,000\,cm^{-1}$, a larger absorption difference ($\Delta\alpha$) between LCP and RCP light gives higher distinguishability (blue line, $\Delta\alpha = 4,000\,cm^{-1}$; red line, $\Delta\alpha = 1,000\,cm^{-1}$). **c** | The photoresponsivity (left) and photoconductor gains (right) of the 1D chiral-perovskite-based circularly polarized photodetectors under LCP and RCP light. R-MBAPbI$_3$-based photodetectors exhibit larger photoresponsivity and photoconductor gains for RCP than for LCP, whereas the opposite is observed for S-MBAPbI$_3$-based photodetectors. **d** | The photoresponsivity of a 2D chiral-perovskite-based circularly polarized photodetector under LCP and RCP light. A similar trend as in panel **c** is observed for the enantiomers (R-MBA)$_2$PbI$_4$ and (S-MBA)$_2$PbI$_4$. Panels **a–c** are reproduced from REF.[38], CC-BY-4.0 (https://creativecommons.org/licenses/by/4.0/). Panel **d** is reproduced with permission from REF.[39], ACS.

Subsequently, polarizing the emission unavoidably reduces its efficiency. Therefore, it is an advantage that chiral-perovskite quantum dots generate single photons with a well-polarized state (circularly polarized). Additionally, it has been shown that chiral materials can be used to detect the orbital angular momentum of light[159], which is another degree of freedom that can be used to record quantum information[160]. Hence, the utilization of chiral perovskites could enable high-capacity quantum communication.

Furthermore, for quantum internet schemes, spins are used as qubits in each node[161] (FIG. 1e), and photons are used to connect these nodes. In this scheme, the spin–photon interface is critical. Recently, it was reported that perovskite quantum dots have a non-degenerate bright triplet exciton state[162,163] that can be used as a spin qubit. Additionally, chiral-perovskite quantum dots interact efficiently with light (they have high absorption coefficients and PLQYs). For these reasons, they may be an ideal platform for spin–photon interfaces and quantum networks. Chiral perovskites may also be used to tune the properties of these spin–photon interfaces. Towards this direction, spin manipulation and characterization of spin coherence times are important future steps.

Lead-free chiral perovskites

Chiral perovskites can also be partially or wholly doped by different heavy metals, resulting in two benefits. One is the direct manipulation of the fundamental properties of the perovskites. A recent review has highlighted the structure–property effects of doping in achiral perovskites[164], which could prove to be a template for the chiral variants. For chiral applications (including spintronic devices), we expect that spin–orbit coupling will play an important role in the design and tuning of the optoelectronic and spintronic properties of chiral perovskites, and the influence of different metals should be dramatic.

The second benefit is the possibility of making lead-free devices. For some applications, the presence of lead is problematic. Lead's toxicity stems from its ability to mimic other metals and interfere with biological functions. Examples include blocking N-methyl-D-aspartate receptors and inhibiting the formation of haem, leading to neuron damage and anaemia, respectively[165].

Therefore, its replacement with a less hazardous metal is strongly desired. For achiral perovskites, tin (Sn^{2+}) is considered to be the most promising alternative[164], as it has a similar ionic radius as lead, and tin-based solar
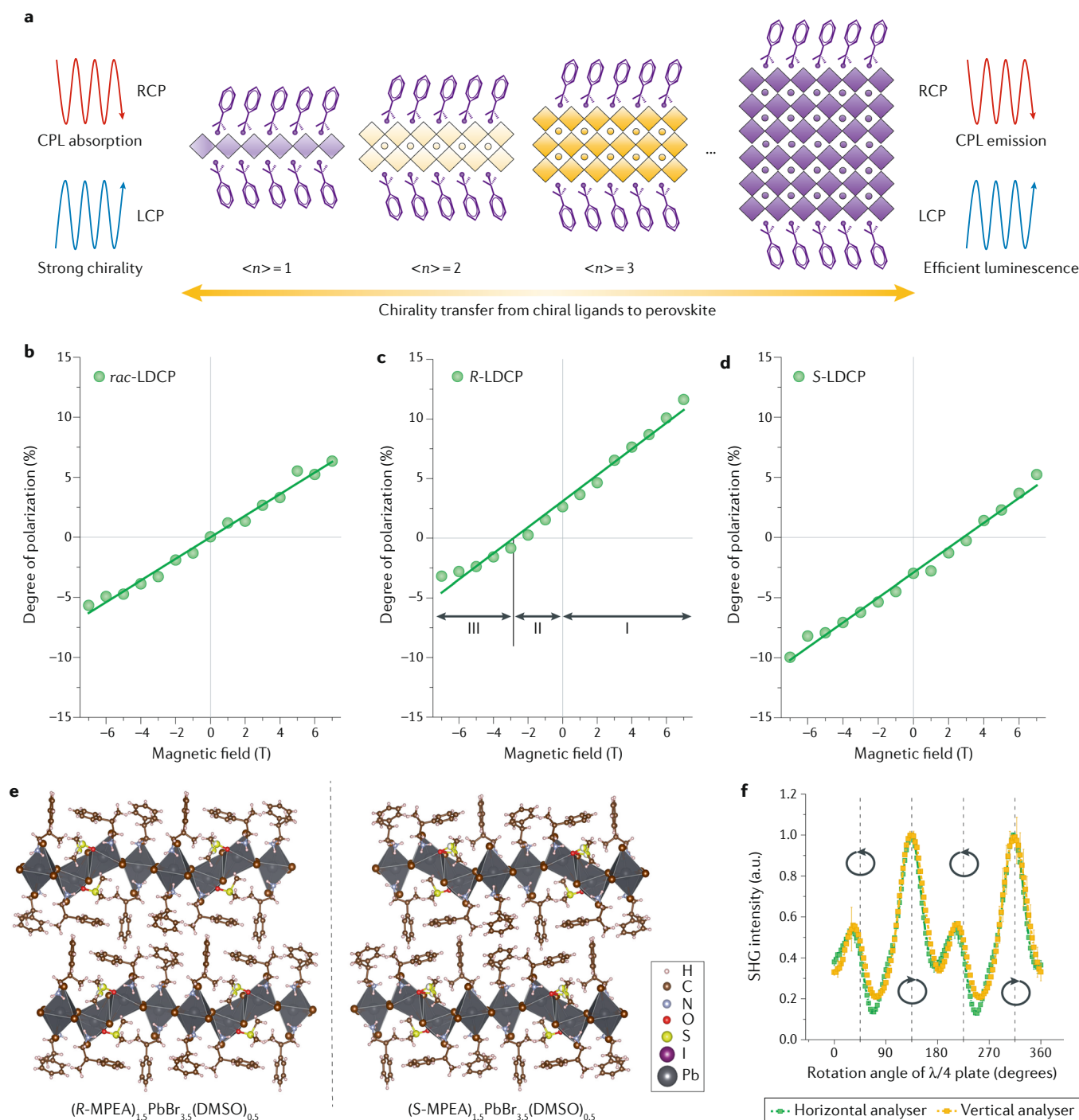
Fig. 7 | **Spin manipulation and nonlinear chiroptical effects in chiral perovskites.** Schematic illustration of the structures of low-dimensional chiral perovskites (LDCPs) with different numbers of inorganic layers (<n>). Smaller <n> gives strong chirality, owing to the large mole fraction of chiral ligands, whereas larger <n> gives strong photoluminescence through energy funnelling. Thus, there is a balance between strong chirality and large photoluminescence quantum yield for LDCPs (panel **a**). The degree of photoluminescence polarization for *rac*-LDCP (panel **b**), *R*-LDCP (panel **c**) and *S*-LDCP (panel **d**) as a function of magnetic field is also shown, accompanied by fits to Eq. 3. The crystal structures of (*R*-MPEA)$_{1.5}$PbBr$_{3.5}$(DMSO)$_{0.5}$ (left) and its enantiomer (*S*-MPEA)$_{1.5}$PbBr$_{3.5}$(DMSO)$_{0.5}$ (right) (panel **e**). Polarization-dependent second-harmonic generation (SHG) for (*R*-MPEA)$_{1.5}$PbBr$_{3.5}$(DMSO)$_{0.5}$ nanowires. By rotating the λ/4 wave plate, the excitation can be modulated from linear polarization to circular polarization (the circular arrows refer to left and right circular polarization). The excitation wavelength is 850 nm and the detection wavelength is 425 nm. Vertical (yellow line) and horizontal (green line) analysers are used to analyse the polarization of the generated SHG signal (panel **f**). CPL, circularly polarized light; LCP, left-handed circularly polarized; RCP, right-handed circularly polarized. Panels **a–d** are adapted from REF.[83], Springer Nature Limited. Panels **e** and **f** are reproduced with permission from REF.[48], ACS.
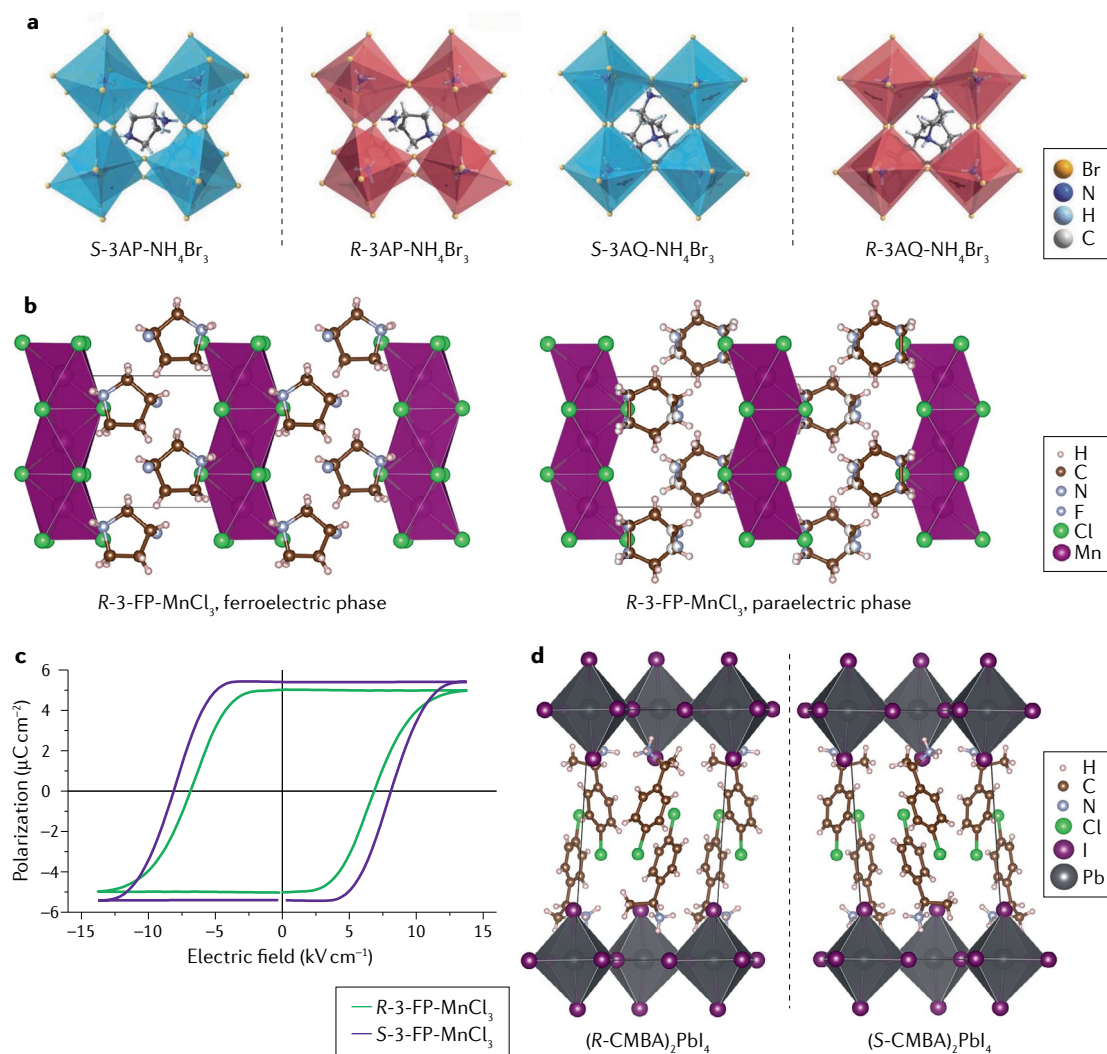
Fig. 8 | **Chiral-perovskite-based ferroelectrics. a** | The crystal structures of S-3AP-NH$_4$Br$_3$ and its enantiomer R-3AP-NH$_4$Br$_3$ (left) and of S-3AQ-NH$_4$Br$_3$ and its enantiomer R-3AQ-NH$_4$Br$_3$ (right) in the ferroelectric phase (space group P2$_1$, measured at 293 K). **b** | The crystal structures of R-3-FP-MnCl$_3$ in the ferroelectric phase (space group P2$_1$, measured at 298 K, left) and in the paraelectric phase (space group C222$_1$, measured at 363 K, right). **c** | Ferroelectric hysteresis loops of R-3-FP-MnCl$_3$ (green) and S-3-FP-MnCl$_3$ (purple) single crystals; measurements were performed along the polar b axis at 313 K. **d** | The crystal structures of (R-CMBA)$_2$PbI$_4$ and its enantiomer (S-CMBA)$_2$PbI$_4$ in the ferroelectric phase (space group P1, measured at 293 K). Panel **a** is reproduced with permission from REF.[84], AAAS. Panels **b** and **c** are reproduced with permission from REF.[41], ACS. Panel **d** is reproduced with permission from REF.[40], Wiley-VCH.

cells have achieved power-conversion efficiencies over 9%[166]. Recently, other lead-free chiral HOIPs based on bismuth[37], copper[106–108], manganese[41] and cobalt[110] have also been reported. Hybrid chiral manganese perovskites are good candidates for circularly polarized LEDs[167] and hybrid chiral copper and cobalt perovskites are attractive chiral ferromagnetic materials[168].

Machine learning and theoretical studies

In recent years, machine learning, in combination with density functional theory, has enabled the computational screening and accelerated the discovery of novel perovskite structures[169–173]. Some lead-free perovskites were predicted by theoretical calculations and then realized synthetically[174,175]. The systematic application of machine learning for the identification of novel chiral-perovskite structures would accelerate discovery, but a larger library of materials is first necessary to gain predictive power. At the same time, deeper theoretical studies are still needed to predict circular dichroism, circularly polarized emission and the topological quantum properties of chiral perovskites[51,176,177]. These theoretical studies could provide more suggestions and guidance for the rational design of high-performance chiral-perovskite materials and accelerate the development of chiroptics towards applications.

New design strategies

The strategies for circumventing the challenges for chiral perovskites might naturally diverge from those that are currently employed. For example, changes that slightly decrease the mobility might still be considered

worthwhile if they greatly increase the circular dichroism. In addition, the desire for chirality will require novel synthetic routes to obtain larger dissymmetry factors; this will result in new structure–property/performance relationships that will influence subsequent developments and applications.

Today, most efforts on chiral HOIPs still focus on bottom-up strategies through molecular design[33,34,84]; however, 3D printing provides another strategy to construct perovskite chiral structures through bottom-up

approaches. Top-down strategies towards chiral-perovskite metasurfaces are also very promising[178–181]. These approaches combine the advantages of metastructures (strong chirality) with the impressive optical, electrical and spintronic properties of perovskites. We envision that both bottom-up and top-down strategies will continue to improve the chiral properties of HOIPs.

Published online: 10 March 2020

1. Shi, D. et al. Low trap-state density and long carrier diffusion in organolead trihalide perovskite single crystals. *Science* **347**, 519–522 (2015).
2. Stranks, S. D. et al. Electron-hole diffusion lengths exceeding 1 micrometer in an organometal trihalide perovskite absorber. *Science* **342**, 341–344 (2013).
3. Xing, G. et al. Long-range balanced electron- and hole-transport lengths in organic-inorganic $CH_3NH_3PbI_3$. *Science* **342**, 344–347 (2013).
4. Dong, Q. et al. Electron-hole diffusion lengths >175 μm in solution-grown $CH_3NH_3PbI_3$ single crystals. *Science* **347**, 967–970 (2015).
5. Tong, J. et al. Carrier lifetimes of >1 μs in Sn-Pb perovskites enable efficient all-perovskite tandem solar cells. *Science* **364**, 475–479 (2019).
6. Eperon, G. E. et al. Perovskite-perovskite tandem photovoltaics with optimized band gaps. *Science* **354**, 861–865 (2016).
7. Tsai, H. et al. High-efficiency two-dimensional Ruddlesden–Popper perovskite solar cells. *Nature* **536**, 312–316 (2016).
8. Jung, E. H. et al. Efficient, stable and scalable perovskite solar cells using poly(3-hexylthiophene). *Nature* **567**, 511–515 (2019).
9. Zhao, D. et al. Efficient two-terminal all-perovskite tandem solar cells enabled by high-quality low-bandgap absorber layers. *Nat. Energy* **3**, 1093–1100 (2018).
10. Yuan, M. et al. Perovskite energy funnels for efficient light-emitting diodes. *Nat. Nanotechnol.* **11**, 872–877 (2016).
11. Wang, N. et al. Perovskite light-emitting diodes based on solution-processed self-organized multiple quantum wells. *Nat. Photon.* **10**, 699–704 (2016).
12. Zhao, B. et al. High-efficiency perovskite–polymer bulk heterostructure light-emitting diodes. *Nat. Photon.* **12**, 783–789 (2018).
13. Li, Z. et al. Room-temperature continuous-wave operation of organometal halide perovskite lasers. *ACS Nano* **12**, 10968–10976 (2018).
14. Xing, G. et al. Low-temperature solution-processed wavelength-tunable perovskites for lasing. *Nat. Mater.* **13**, 476–480 (2014).
15. Zhu, H. et al. Lead halide perovskite nanowire lasers with low lasing thresholds and high quality factors. *Nat. Mater.* **14**, 636–642 (2015).
16. Zhang, Q., Ha, S. T., Liu, X., Sum, T. C. & Xiong, Q. Room-temperature near-infrared high-Q perovskite whispering-gallery planar nanolasers. *Nano Lett.* **14**, 5995–6001 (2014).
17. Zhang, H. et al. 2D Ruddlesden–Popper perovskites microring laser array. *Adv. Mater.* **30**, 1706186 (2018).
18. Milot, R. L. et al. Charge-carrier dynamics in 2D hybrid metal–halide perovskites. *Nano Lett.* **16**, 7001–7007 (2016).
19. Senanayak, S. P. et al. Understanding charge transport in lead iodide perovskite thin-film field-effect transistors. *Sci. Adv.* **3**, e1601935 (2017).
20. Kagan, C. R., Mitzi, D. B. & Dimitrakopoulos, C. D. Organic-inorganic hybrid materials as semiconducting channels in thin-film field-effect transistors. *Science* **286**, 945–947 (1999).
21. Brenner, T. M., Egger, D. A., Kronik, L., Hodes, G. & Cahen, D. Hybrid organic–inorganic perovskites: low-cost semiconductors with intriguing charge-transport properties. *Nat. Rev. Mater.* **1**, 15007 (2016).
22. Juarez-Perez, E. J. et al. Photoinduced giant dielectric constant in lead halide perovskite solar cells. *J. Phys. Chem. Lett.* **5**, 2390–2394 (2014).
23. Lin, Q., Armin, A., Burn, P. L. & Meredith, P. Filterless narrowband visible photodetectors. *Nat. Photon.* **9**, 687–694 (2015).
24. Fang, Y., Dong, Q., Shao, Y., Yuan, Y. & Huang, J. Highly narrowband perovskite single-crystal photodetectors enabled by surface-charge recombination. *Nat. Photon.* **9**, 679–686 (2015).
25. Niesner, D. et al. Giant Rashba splitting in $CH_3NH_3PbBr_3$ organic-inorganic perovskite. *Phys. Rev. Lett.* **117**, 126401 (2016).
26. Mosconi, E., Etienne, T. & De Angelis, F. Rashba band splitting in organohalide lead perovskites: bulk and surface effects. *J. Phys. Chem. Lett.* **8**, 2247–2252 (2017).
27. Odenthal, P. et al. Spin-polarized exciton quantum beating in hybrid organic–inorganic perovskites. *Nat. Phys.* **13**, 894–899 (2017).
28. Giovanni, D. et al. Highly spin-polarized carrier dynamics and ultralarge photoinduced magnetization in $CH_3NH_3PbI_3$ perovskite thin films. *Nano Lett.* **15**, 1553–1558 (2015).
29. Zheng, F., Tan, L. Z., Liu, S. & Rappe, A. M. Rashba spin-orbit coupling enhanced carrier lifetime in $CH_3NH_3PbI_3$. *Nano Lett.* **15**, 7794–7800 (2015).
30. Wang, J. et al. Spin-optoelectronic devices based on hybrid organic-inorganic trihalide perovskites. *Nat. Commun.* **10**, 129 (2019).
31. Sun, D. et al. Spintronics of organometal trihalide perovskites. Preprint at *arXiv* https://arxiv.org/abs/1608.00993 (2016).
32. Liao, K. et al. Spintronics of hybrid organic–inorganic perovskites: miraculous basis of integrated optoelectronic devices. *Adv. Opt. Mater.* **7**, 1900350 (2019).
33. Billing, D. G. & Lemmerer, A. Bis[(*S*)-β-phenethylammonium] tribromoplumbate(II). *Acta Cryst. E* **59**, m381–m383 (2003).
   The first report of a chiral organic–inorganic perovskite.
34. Billing, D. G. & Lemmerer, A. Synthesis and crystal structures of inorganic–organic hybrids incorporating an aromatic amine with a chiral functional group. *CrystEngComm* **8**, 686–695 (2006).
35. Peng, Y. et al. White-light emission in a chiral one-dimensional organic–inorganic hybrid perovskite. *J. Mater. Chem. C* **6**, 6033–6037 (2018).
36. Mercier, N. et al. Conglomerate-to-true-racemate reversible solid-state transition in crystals of an organic disulfide-based iodoplumbate. *Angew. Chem. Int. Ed.* **45**, 2100–2103 (2006).
37. Moon, T. H., Oh, S.-J. & Ok, K. M. [((*R*)-$C_8H_{12}N$)$_4$][Bi_2Br_{10}] and [((*S*)-$C_8H_{12}N$)$_4$][Bi_2Br_{10}]: chiral hybrid bismuth bromides templated by chiral organic cations. *ACS Omega* **3**, 17895–17903 (2018).
38. Chen, C. et al. Circularly polarized light detection using chiral hybrid perovskite. *Nat. Commun.* **10**, 1927 (2019).
   Report of chiral-perovskite photodetectors with responsivity 100 times higher than that of chiral-metasurface photodetectors.
39. Ma, J. et al. Chiral 2D perovskites with a high degree of circularly polarized photoluminescence. *ACS Nano* **13**, 3659–3665 (2019).
   Report of ∼17% photoluminescence polarization of 2D chiral-perovskite microplates at 77 K.
40. Yang, C.-K. et al. The first 2D homochiral lead iodide perovskite ferroelectrics: [*R*- and *S*-1-(4-chlorophenyl) ethylammonium]$_2PbI_4$. *Adv. Mater.* **31**, 1808088 (2019).
41. Ai, Y. et al. Fluorine substitution induced high T_c of enantiomeric perovskite ferroelectrics: (*R*)- and (*S*)-3-(fluoropyrrolidinium)$MnCl_3$. *J. Am. Chem. Soc.* **141**, 4474–4479 (2019).
42. Liu, Y. et al. Chemical nature of ferroelastic twin domains in $CH_3NH_3PbI_3$ perovskite. *Nat. Mater.* **17**, 1013–1019 (2018).
43. Abendroth, J. M. et al. Spin selectivity in photoinduced charge-transfer mediated by chiral molecules. *ACS Nano* **13**, 4928–4946 (2019).
44. Naaman, R., Paltiel, Y. & Waldeck, D. H. Chiral molecules and the electron spin. *Nat. Rev. Chem.* **3**, 250–260 (2019).
   Comprehensive review of chiral-induced spin-selective effect and its applications.
45. Kelvin, W. T. *The Molecular Tactics of a Crystal* 26–27 (Clarendon, 1894).
46. Berova, N., Nakanishi, K. & Woody, R. W. (eds) *Circular Dichroism: Principles and Applications* 2nd edn (Wiley-VCH, 2000).
47. Ahn, J. et al. A new class of chiral semiconductors: chiral-organic-molecule-incorporating organic–inorganic hybrid perovskites. *Mater. Horiz.* **4**, 851–856 (2017).
   First exploration of chiroptical behaviour of chiral organic–inorganic perovskites by circular dichroism.
48. Yuan, C. et al. Chiral lead halide perovskite nanowires for second-order nonlinear optics. *Nano Lett.* **18**, 5411–5417 (2018).
   Report of circularly polarized SHG in chiral-perovskite nanowires.
49. Naciri, J. et al. Synthesis and pyroelectric properties of novel ferroelectric organosiloxane liquid crystalline materials. *Chem. Mater.* **14**, 5134–5139 (2002).
50. Zhang, H.-Y., Tang, Y.-Y., Shi, P.-P. & Xiong, R.-G. Toward the targeted design of molecular ferroelectrics: modifying molecular symmetries and homochirality. *Acc. Chem. Res.* **52**, 1928–1938 (2019).
51. Sanchez, D. S. et al. Topological chiral crystals with helicoid-arc quantum states. *Nature* **567**, 500–505 (2019).
52. Yang, Y., da Costa, R. C., Fuchter, M. J. & Campbell, A. J. Circularly polarized light detection by a chiral organic semiconductor transistor. *Nat. Photon.* **7**, 634–638 (2013).
53. Li, W. et al. Circularly polarized light detection with hot electrons in chiral plasmonic metamaterials. *Nat. Commun.* **6**, 8379 (2015).
54. Brandt, J. R., Salerno, F. & Fuchter, M. J. The added value of small-molecule chirality in technological applications. *Nat. Rev. Chem.* **1**, 0045 (2017).
55. Schulz, M. et al. Chiral excitonic organic photodiodes for direct detection of circular polarized light. *Adv. Funct. Mater.* **29**, 1900684 (2019).
56. Wu, Z.-G. et al. Chiral octahydro-binaphthol compound-based thermally activated delayed fluorescence materials for circularly polarized electroluminescence with superior EQE of 32.6% and extremely low efficiency roll-off. *Adv. Mater.* **31**, 1900524 (2019).
57. Zinna, F. et al. Design of lanthanide-based OLEDs with remarkable circularly polarized electroluminescence. *Adv. Funct. Mater.* **27**, 1603719 (2017).
58. Feuillastre, S. et al. Design and synthesis of new circularly polarized thermally activated delayed fluorescence emitters. *J. Am. Chem. Soc.* **138**, 3990–3993 (2016).
59. Yang, Y., da Costa, R. C., Smilgies, D.-M., Campbell, A. J. & Fuchter, M. J. Induction of circularly polarized electroluminescence from an achiral light-emitting polymer via a chiral small-molecule dopant. *Adv. Mater.* **25**, 2624–2628 (2013).
60. Han, J. et al. Recent progress on circularly polarized luminescent materials for organic optoelectronic devices. *Adv. Opt. Mater.* **6**, 1800538 (2018).
61. Kissick, D. J., Wanapun, D. & Simpson, G. J. Second-order nonlinear optical imaging of chiral crystals. *Annu. Rev. Anal. Chem.* **4**, 419–437 (2011).
62. Heffern, M. C., Matosziuk, L. M. & Meade, T. J. Lanthanide probes for bioresponsive imaging. *Chem. Rev.* **114**, 4496–4539 (2014).
63. Lee, H. et al. Chiral imaging of collagen by second-harmonic generation circular dichroism. *Biomed. Opt. Express* **4**, 909–916 (2013).

64. Bisoyi, H. K. & Li, Q. Light-directing chiral liquid crystal nanostructures: from 1D to 3D. *Acc. Chem. Res.* **47**, 3184–3195 (2014).

65. Schadt, M. Liquid crystal materials and liquid crystal displays. *Annu. Rev. Mater. Sci.* **27**, 305–379 (1997).

66. Nielsen, M. A. & Chuang, I. L. *Quantum Computation and Quantum Information: 10th Anniversary Edition* (Cambridge Univ. Press, 2011).

67. Service, R. F. Ultrafast lasers. Lighting the way to a quantum computer. *Science* **292**, 2412–2413 (2001).

68. Gisin, N. & Thew, R. Quantum communication. *Nat. Photon.* **1**, 165–171 (2007).

69. Liao, S.-K. et al. Satellite-relayed intercontinental quantum network. *Phys. Rev. Lett.* **120**, 030501 (2018).

70. Humphreys, P. C. et al. Deterministic delivery of remote entanglement on a quantum network. *Nature* **558**, 268–273 (2018).

71. Chang, K. et al. Discovery of robust in-plane ferroelectricity in atomic-thick SnTe. *Science* **353**, 274–278 (2016).

72. Kepenekian, M. et al. Rashba and Dresselhaus effects in hybrid organic–inorganic perovskites: from basics to devices. *ACS Nano* **9**, 11557–11567 (2015).

73. Lee, D.-M., Song, J.-W., Lee, Y.-J., Yu, C.-J. & Kim, J.-H. Control of circularly polarized electroluminescence in induced twist structure of conjugate polymer. *Adv. Mater.* **29**, 1700907 (2017).

74. Wan, L. et al. Inverting the handedness of circularly polarized luminescence from light-emitting polymers using film thickness. *ACS Nano* **13**, 8099–8105 (2019).

75. Dor, O. B., Yochelis, S., Mathew, S. P., Naaman, R. & Paltiel, Y. A chiral-based magnetic memory device without a permanent magnet. *Nat. Commun.* **4**, 2256 (2013).

76. Ben Dor, O. et al. Magnetization switching in ferromagnets by adsorbed chiral molecules without current or external magnetic field. *Nat. Commun.* **8**, 14567 (2017).

77. Lee, M. M., Teuscher, J., Miyasaka, T., Murakami, T. N. & Snaith, H. J. Efficient hybrid solar cells based on meso-superstructured organometal halide perovskites. *Science* **338**, 643–647 (2012).

78. Kim, H.-S. et al. Lead iodide perovskite sensitized all-solid-state submicron thin film mesoscopic solar cell with efficiency exceeding 9%. *Sci. Rep.* **2**, 591 (2012).

79. He, T. et al. Spectroscopic studies of chiral perovskite nanocrystals. *Appl. Phys. Lett.* **111**, 151102 (2017).

80. Chen, W. et al. Two-photon absorption-based upconverted circularly polarized luminescence generated in chiral perovskite nanocrystals. *J. Phys. Chem. Lett.* **10**, 3290–3295 (2019). **Report of the first TP-UCPPL**.

81. Shi, Y., Duan, P., Huo, S., Li, Y. & Liu, M. Endowing perovskite nanocrystals with circularly polarized luminescence. *Adv. Mater.* **30**, 1705011 (2018).

82. Georgieva, Z. N., Bloom, B. P., Ghosh, S. & Waldeck, D. H. Imprinting chirality onto the electronic states of colloidal perovskite nanoplatelets. *Adv. Mater.* **30**, 1800097 (2018).

83. Long, G. et al. Spin control in reduced-dimensional chiral perovskites. *Nat. Photon.* **12**, 528–533 (2018). **Report of low-dimensional chiral perovskites exhibiting 3% circularly polarized photoluminescence without an external magnetic field**.

84. Ye, H.-Y. et al. Metal-free three-dimensional perovskite ferroelectrics. *Science* **361**, 151–155 (2018). **Report of the first metal-free 3D chiral perovskites**.

85. Long, G. et al. Theoretical prediction of chiral 3D hybrid organic–inorganic perovskites. *Adv. Mater.* **31**, 1807628 (2019). **Theoretical prediction that 3D chiral organic–inorganic perovskites are thermodynamically and kinetically stable**.

86. Sohncke, L. *Entwickelung einer Theorie der Krystallstruktur* (Teubner, 1879).

87. Neumann, F. E. & Meyer, O. E. *Vorlesungen über die Theorie der Elasticität der festen Körper und des Lichtäthers, gehalten an der Universität Königsberg* (Teubner, 1885).

88. Curie, P. Sur la symêtrie dans les phênomènes physiques, symêtrie d'un champ électrique et d'un champ magnétique. *J. Phys. Theor. Appl.* **3**, 393–415 (1894).

89. Dong, Y. et al. Chiral perovskites: promising materials toward next-generation optoelectronics. *Small* **15**, 1902237 (2019).

90. Fischer, P. & Hache, F. Nonlinear optical spectroscopy of chiral molecules. *Chirality* **17**, 421–437 (2005).

91. Shi, P.-P. et al. Symmetry breaking in molecular ferroelectrics. *Chem. Soc. Rev.* **45**, 3811–3827 (2016).

92. Mujica, V. Chirality transfer takes a jump. *Nat. Chem.* **7**, 543–544 (2015).

93. Ostovar pour, S. et al. Through-space transfer of chiral information mediated by a plasmonic nanomaterial. *Nat. Chem.* **7**, 591–596 (2015).

94. Ma, W. et al. Chiral inorganic nanostructures. *Chem. Rev.* **117**, 8041–8093 (2017).

95. Li, Y., Yu, D., Dai, L., Urbas, A. & Li, Q. Organo-soluble chiral thiol-monolayer-protected gold nanorods. *Langmuir* **27**, 98–103 (2011).

96. Dolamic, I., Knoppe, S., Dass, A. & Bürgi, T. First enantioseparation and circular dichroism spectra of Au$_{38}$ clusters protected by achiral ligands. *Nat. Commun.* **3**, 798 (2012).

97. Goldsmith, M.-R. et al. The chiroptical signature of achiral metal clusters induced by dissymmetric adsorbates. *Phys. Chem. Chem. Phys.* **8**, 63–67 (2006).

98. Carmeli, I. et al. Broad band enhancement of light absorption in photosystem I by metal nanoparticle antennas. *Nano Lett.* **10**, 2069–2074 (2010).

99. Lemmerer, A. & Billing, D. G. Inorganic–organic hybrids incorporating a chiral cyclic ammonium cation. *S. Afr. J. Chem.* **66**, 263–272 (2013).

100. Yuan, Z. et al. One-dimensional organic lead halide perovskites with efficient bluish white-light emission. *Nat. Commun.* **8**, 14051 (2017).

101. Hu, T. et al. Mechanism for broadband white-light emission from two-dimensional (110) hybrid perovskites. *J. Phys. Chem. Lett.* **7**, 2258–2263 (2016).

102. Peng, Y. et al. Exploration of chiral organic–inorganic hybrid semiconducting lead halides. *Chem. Asian J.* **14**, 2273–2277 (2019).

103. Zhu, L.-L. et al. Stereochemically active lead chloride enantiomers mediated by homochiral organic cation. *Polyhedron* **158**, 445–448 (2019).

104. Black, R. S. & Billing, D. G. The structure and photoluminescence of chiral tin and lead inorganic-organic hybrid perovskites. *Acta Cryst. A* **64**, C455–C456 (2008).

105. Black, R. S. *Structure and Optical Properties of Natural Low Dimensional, Semiconducting, Organic Inorganic Hybrids*. Thesis, Univ. Witwatersrand (2012).

106. Hajlaoui, F. et al. Synthesis, crystal structures, second harmonic generation response and temperature phase transitions of two noncentrosymmetric Cu(II)-hybrid halides compounds: [(R)-C$_7$H$_{16}$N$_2$][CuX$_4$] (X = Cl or Br). *J. Mol. Struct.* **1182**, 47–53 (2019).

107. Ben Salah, A. M., Sayari, N., Naïli, H. & Norquist, A. J. Chiral and achiral copper(II) complexes: structure, bonding and biological activities. *RSC Adv.* **6**, 59055–59065 (2016).

108. Mande, H. M., Ghalsasi, P. S. & Navamoney, A. Synthesis, structural and spectroscopic characterization of the thermochromic compounds A$_2$CuCl$_4$: [(naphthyl ethylammonium)$_2$CuCl$_4$]. *Polyhedron* **91**, 141–149 (2015).

109. Tang, Y.-Y. et al. H/F-substitution-induced homochirality for designing high-T_c molecular perovskite ferroelectrics. *Adv. Mater.* **31**, 1902163 (2019).

110. Mande, H. M., Ghalsasi, P. S. & Arulsamy, N. Racemic and conglomerate 1-(4-haloaryl)ethylammonium tetrachlorocobaltate salts: formation of helical structures. *RSC Adv.* **5**, 62719–62723 (2015).

111. Gao, X., Han, B., Yang, X. & Tang, Z. Perspective of chiral colloidal semiconductor nanocrystals: opportunity and challenge. *J. Am. Chem. Soc.* **141**, 13700–13707 (2019).

112. Tong, Y. et al. Highly luminescent cesium lead halide perovskite nanocrystals with tunable composition and thickness by ultrasonication. *Angew. Chem. Int. Ed.* **55**, 13887–13892 (2016).

113. Xue, S., Xing, P., Zhang, J., Zeng, Y. & Zhao, Y. Diverse role of solvents in controlling supramolecular chirality. *Chem. Eur. J.* **25**, 7426–7437 (2019).

114. Rickhaus, M., Mayor, M. & Juríček, M. Strain-induced helical chirality in polyaromatic systems. *Chem. Soc. Rev.* **45**, 1542–1556 (2016).

115. Kuzyk, A. et al. DNA-based self-assembly of chiral plasmonic nanostructures with tailored optical response. *Nature* **483**, 311–314 (2012).

116. Yashima, E. et al. Supramolecular helical systems: helical assemblies of small molecules, foldamers, and polymers with chiral amplification and their functions. *Chem. Rev.* **116**, 13752–13990 (2016).

117. Huck, N. P. M., Jager, W. F., de Lange, B. & Feringa, B. L. Dynamic control and amplification of molecular chirality by circular polarized light. *Science* **273**, 1686–1688 (1996).

118. Moss, G. P. Basic terminology of stereochemistry (IUPAC Recommendations 1996). *Pure Appl. Chem.* **68**, 2193–2222 (1996).

119. Zhao, H.-R., Li, D.-P., Ren, X.-M., Song, Y. & Jin, W.-Q. Larger spontaneous polarization ferroelectric inorganic – organic hybrids: [PbI$_3$]$_\infty$ chains directed organic cations aggregation to kagomé-shaped tubular architecture. *J. Am. Chem. Soc.* **132**, 18–19 (2010).

120. Zheng, H. et al. Uncovering the circular polarization potential of chiral photonic cellulose films for photonic applications. *Adv. Mater.* **30**, 1705948 (2018).

121. Schellman, J. A. & Oriel, P. Origin of the cotton effect of helical polypeptides. *J. Chem. Phys.* **37**, 2114–2124 (1962).

122. Rochat, E., Walker, S. D. & Parker, M. C. Polarisation and wavelength division multiplexing at 1.55 μm for bandwidth enhancement of multimode fibre based access networks. *Opt. Express* **12**, 2280–2292 (2004).

123. Yang, Y. et al. Emergent properties of an organic semiconductor driven by its molecular chirality. *ACS Nano* **11**, 8329–8338 (2017).

124. Liu, H. L. et al. 3D chiral color prints for anti-counterfeiting. *Nanoscale* **11**, 5506–5511 (2019).

125. Brandt, J. R., Wang, X., Yang, Y., Campbell, A. J. & Fuchter, M. J. Circularly polarized phosphorescent electroluminescence with a high dissymmetry factor from PHOLEDs based on a platinahelicene. *J. Am. Chem. Soc.* **138**, 9743–9746 (2016).

126. Cao, Y. et al. Perovskite light-emitting diodes based on spontaneously formed submicrometre-scale structures. *Nature* **562**, 249–253 (2018).

127. Lin, K. et al. Perovskite light-emitting diodes with external quantum efficiency exceeding 20 per cent. *Nature* **562**, 245–248 (2018).

128. Xing, G. et al. Transcending the slow bimolecular recombination in lead-halide perovskites for electroluminescence. *Nat. Commun.* **8**, 14558 (2017).

129. Zhang, C. et al. Magnetic field effects in hybrid perovskite devices. *Nat. Phys.* **11**, 427–434 (2015).

130. Hilborn, R. C. Einstein coefficients, cross sections, *f* values, dipole moments, and all that. *Am. J. Phys.* **50**, 982–986 (1982).

131. Minzioni, P. et al. Roadmap on all-optical processing. *J. Opt.* **21**, 063001 (2019).

132. Zipfel, W. R., Williams, R. M & Webb, W. W. Nonlinear magic: multiphoton microscopy in the biosciences. *Nat. Biotechnol.* **21**, 1369–1377 (2003).

133. Halasyamani, P. S. & Poeppelmeier, K. R. Noncentrosymmetric oxides. *Chem. Mater.* **10**, 2753–2769 (1998).

134. Stoumpos, C. C. et al. Ruddlesden–Popper hybrid lead iodide perovskite 2D homologous semiconductors. *Chem. Mater.* **28**, 2852–2867 (2016).

135. Li, L. et al. Bilayered hybrid perovskite ferroelectric with giant two-photon absorption. *J. Am. Chem. Soc.* **140**, 6806–6809 (2018).

136. Gao, Y. et al. Electro-optic modulation in hybrid metal halide perovskites. *Adv. Mater.* **31**, 1808336 (2019).

137. Kalanoor, B. S. et al. Third-order optical nonlinearities in organometallic methylammonium lead iodide perovskite thin films. *ACS Photon.* **3**, 361–370 (2016).

138. Zhang, R. et al. Nonlinear optical response of organic–inorganic halide perovskites. *ACS Photon.* **3**, 371–377 (2016).

139. Quan, L. N., Kang, J., Ning, C.-Z. & Yang, P. Nanowires for photonics. *Chem. Rev.* **119**, 9153–9169 (2019).

140. Fu, Y. et al. Metal halide perovskite nanostructures for optoelectronic applications and the study of physical properties. *Nat. Rev. Mater.* **4**, 169–188 (2019).

141. Abel, S. et al. Large Pockels effect in micro- and nanostructured barium titanate integrated on silicon. *Nat. Mater.* **18**, 42–47 (2019).

142. Fang, L. et al. Ultra-directional high-efficiency chiral silicon photonic circuits. *Optica* **6**, 61–66 (2019).

143. Olesiak-Banska, J., Waszkielewicz, M., Obstarczyk, P. & Samoc, M. Two-photon absorption and photoluminescence of colloidal gold nanoparticles and nanoclusters. *Chem. Soc. Rev.* **48**, 4087–4117 (2019).

144. Yang, X., Yang, M., Pang, B., Vara, M. & Xia, Y. Gold nanomaterials at work in biomedicine. *Chem. Rev.* **115**, 10410–10488 (2015).

145. Boyd, R. W. in *Nonlinear Optics* 3rd edn 69–133 (Academic, 2008).

146. Scott, J. F. Applications of modern ferroelectrics. *Science* **315**, 954–959 (2007).

147. Chen, A. A review of emerging non-volatile memory (NVM) technologies and applications. *Solid State Electron.* **125**, 25–38 (2016).

148. Zhang, Y. et al. Highly efficient red-light emission in an organic–inorganic hybrid ferroelectric: (pyrrolidinium) MnCl$_3$. *J. Am. Chem. Soc.* **137**, 4928–4931 (2015).

149. Tang, Y.-Y. et al. Multiaxial molecular ferroelectric thin films bring light to practical applications. *J. Am. Chem. Soc.* **140**, 8051–8059 (2018).

150. Huang, P.-J., Taniguchi, K. & Miyasaka, H. Bulk photovoltaic effect in a pair of chiral–polar layered perovskite-type lead iodides altered by chirality of organic cations. *J. Am. Chem. Soc.* **141**, 14520–14523 (2019).

151. Huang, S. et al. Halogenated-methylammonium based 3D halide perovskites. *Adv. Mater.* **31**, 1903830 (2019).

152. Guy, S., Baguenard, B., Bensalah-Ledoux, A., Hadiouche, D. & Guy, L. Full polarization control of optical planar waveguides with chiral material. *ACS Photon.* **4**, 2916–2922 (2017).

153. Cerdán, L. et al. Circularly polarized laser emission in optically active organic dye solutions. *Phys. Chem. Chem. Phys.* **19**, 22088–22093 (2017).

154. Niesner, D. et al. Structural fluctuations cause spin-split states in tetragonal (CH₃NH₃)PbI₃ as evidenced by the circular photogalvanic effect. *Proc. Natl Acad. Sci. USA* **115**, 9509–9514 (2018).

155. Xiao, D., Liu, G.-B., Feng, W., Xu, X. & Yao, W. Coupled spin and valley physics in monolayers of MoS_2 and other group-VI dichalcogenides. *Phys. Rev. Lett.* **108**, 196802 (2012).

156. Srivastava, A. et al. Valley Zeeman effect in elementary optical excitations of monolayer WSe_2. *Nat. Phys.* **11**, 141–147 (2015).

157. Lodahl, P. et al. Chiral quantum optics. *Nature* **541**, 473–480 (2017).

158. Bayer, M. et al. Fine structure of neutral and charged excitons in self-assembled In(Ga)As/(Al)GaAs quantum dots. *Phys. Rev. B* **65**, 195315 (2002).

159. Woźniak, P., De Leon, I., Höflich, K., Leuchs, G. & Banzer, P. Interaction of light carrying orbital angular momentum with a chiral dipolar scatterer. *Optica* **6**, 961–965 (2019).

160. Mirhosseini, M. et al. High-dimensional quantum cryptography with twisted light. *New J. Phys.* **17**, 033033 (2015).

161. Kimble, H. J. The quantum internet. *Nature* **453**, 1023–1030 (2008).

162. Becker, M. A. et al. Bright triplet excitons in caesium lead halide perovskites. *Nature* **553**, 189–193 (2018).

163. Tamarat, P. et al. The ground exciton state of formamidinium lead bromide perovskite nanocrystals is a singlet dark state. *Nat. Mater.* **18**, 717–724 (2019).

164. Zhang, X., Li, L., Sun, Z. & Luo, J. Rational chemical doping of metal halide perovskites. *Chem. Soc. Rev.* **48**, 517–539 (2019).

165. Sanders, T., Liu, Y., Buchner, V. & Tchounwou, P. B. Neurotoxic effects and biomarkers of lead exposure: a review. *Rev. Environ. Health* **24**, 15–46 (2009).

166. Jokar, E., Chien, C.-H., Tsai, C.-M., Fathi, A. & Diau, E. W.-G. Robust tin-based perovskite solar cells with hybrid organic cations to attain efficiency approaching 10%. *Adv. Mater.* **31**, 1804835 (2019).

167. Xu, L.-J., Sun, C.-Z., Xiao, H., Wu, Y. & Chen, Z.-N. Green-light-emitting diodes based on tetrabromide manganese(II) complex through solution process. *Adv. Mater.* **29**, 1605739 (2017).

168. Mitzi, D. B. Synthesis, structure, and properties of organic-inorganic perovskites and related materials. *Prog. Inorg. Chem.* **48**, 1–121 (2007).

169. Lu, S. et al. Accelerated discovery of stable lead-free hybrid organic-inorganic perovskites via machine learning. *Nat. Commun.* **9**, 3405 (2018).

170. Kim, C., Huan, T. D., Krishnan, S. & Ramprasad, R. A hybrid organic-inorganic perovskite dataset. *Sci. Data* **4**, 170057 (2017).

171. Körbel, S., Marques, M. A. L. & Botti, S. Stability and electronic properties of new inorganic perovskites from high-throughput ab initio calculations. *J. Mater. Chem. C.* **4**, 3157–3167 (2016).

172. Takahashi, K., Takahashi, L., Miyazato, I. & Tanaka, Y. Searching for hidden perovskite materials for photovoltaic systems by combining data science and first principle calculations. *ACS Photon.* **5**, 771–775 (2018).

173. Davies, D. W. et al. Computational screening of all stoichiometric inorganic materials. *Chem* **1**, 617–627 (2016).

174. Shi, Z. J. et al. Lead-free organic–inorganic hybrid perovskites for photovoltaic applications: recent advances and perspectives. *Adv. Mater.* **29**, 1605005 (2017).

175. Xiao, Z., Song, Z. & Yan, Y. From lead halide perovskites to lead-free metal halide perovskites and perovskite derivatives. *Adv. Mater.* **31**, 1803792 (2019).

176. Yu, Z.-G. Oscillatory magnetic circular dichroism of free-carrier absorption and determination of the Rashba dispersions in hybrid organic–inorganic perovskites. *J. Phys. Chem. Lett.* **9**, 1–7 (2018).

177. Tepliakov, N. V. et al. Optical activity and circular dichroism of perovskite quantum-dot molecules. *J. Phys. Chem. C.* **123**, 2658–2664 (2019).

178. Gholipour, B. et al. Organometallic perovskite metasurfaces. *Adv. Mater.* **29**, 1604268 (2017).

179. Wang, Z., Wang, Y., Adamo, G., Teng, J. & Sun, H. Induced optical chirality and circularly polarized emission from achiral CdSe/ZnS quantum dots via resonantly coupling with plasmonic chiral metasurfaces. *Laser Photonics Rev.* **13**, 1800276 (2019).

180. Makarov, S. V. et al. Multifold emission enhancement in nanoimprinted hybrid perovskite metasurfaces. *ACS Photon.* **4**, 728–735 (2017).

181. Zhang, C. et al. Lead halide perovskite-based dynamic metasurfaces. *Laser Photonics Rev.* **13**, 1900079 (2019).

182. Nespolo, M., Aroyo, M. I. & Souvignier, B. Crystallographic shelves: space-group hierarchy explained. *J. Appl. Crystallogr.* **51**, 1481–1491 (2018).

183. Lightner, D. A. & Gurst, J. E. *Organic Conformational Analysis and Stereochemistry from Circular Dichroism Spectroscopy* (Wiley-VCH, 2000).

184. Polavarapu, P. L. Kramers – Kronig transformation for optical rotatory dispersion studies. *J. Phys. Chem. A* **109**, 7013–7023 (2005).

185. Li, A. D. & Liu, W. C. in *Physical Properties and Applications of Polymer Nanocomposites* (eds Tjong, S. C. & Mai, Y.-W.) 108–158 (Woodhead, 2010).

186. Liao, W.-Q., Tang, Y.-Y., Li, P.-F., You, Y.-M. & Xiong, R.-G. Competitive halogen bond in the molecular ferroelectric with large piezoelectric response. *J. Am. Chem. Soc.* **140**, 3975–3980 (2018).

Author contributions

W.G., G.K.L. and E.H.S. discussed the content. G.K.L. researched the data for the article, with help from R.S. and M.I.S. All authors contributed to the review and editing of the manuscript.

Competing interests

The authors declare no competing interests.

Publisher's note

Springer Nature remains neutral with regard to jurisdictional claims in published maps and institutional affiliations.

Supplementary information

Supplementary information is available for this paper at https://doi.org/10.1038/s41578-020-0181-5.